

Magnetic-flux quanta in superconducting thin films observed by electron holography and digital phase analysis

Shuji Hasegawa,* Tsuyoshi Matsuda, Junji Endo, Nobuyuki Osakabe, Masukazu Igarashi, Toshio Kobayashi, Masayoshi Naito, and Akira Tonomura
Advanced Research Laboratory, Hitachi, Ltd., Hatoyama, Saitama 350-03, Japan

Ryozo Aoki

Department of Electrical Engineering, Faculty of Engineering, Osaka University, Yamadaoka, Suita 565, Japan
(Received 27 August 1990; revised manuscript received 17 December 1990)

Singly quantized magnetic fluxes in superconducting lead films have been directly observed in the form of magnetic-flux-line distributions by using an electron-holography technique. Combining this with the digital-phase-analysis method, we were able to determine the flux quantum $h/2e$ for individual fluxes with a precision of $\sim h/100e$, and analyze the distributions of field-vector components around the fluxon centers. The internal-field distributions obtained were compared with those calculated from the Ginzburg-Landau equations with use of some models, and an overall agreement was found between them. We also observed the changes of the magnetic-flux structures of lead thin films as a function of their thickness. Fluxon pairs were observed in $0.2\text{-}\mu\text{m}$ -thick films, which may correspond to those suggested by Kosterlitz-Thouless theory.

I. INTRODUCTION

An essential character of superconductivity which has manifested itself in macroscopic quantum state is magnetic-flux quantization in units of $\Phi_0 = h/2e$ (fluxon), a ratio between two universal constants. An exact measurement of the quantity Φ_0 and analysis of the internal structure of a fluxon, therefore are of great importance for basic research on superconductivity.^{1,2} Fluxons form a flux-line lattice in type-II superconductors under external magnetic fields, and they are forced to move by transport currents. When its electromagnetic driving force exceeds the fluxon pinning force, the fluxon starts to move in viscous flow with energy dissipation, resulting in Ohmic resistance and thus limiting the superconducting critical current. Investigation of the static and dynamic behaviors of the fluxons, therefore, play an important role for basic research as well as for industrial applications of superconductors.

As reviewed in Sec. II various kinds of experimental techniques have been employed for the observation of fluxons since the prediction of Abrikosov. Although, especially, the methods using electron waves such as Lorentz microscopy were considered powerful, they have not yet attained fully satisfactory results, because the observation had to be carried out near the measurement limitation from the uncertainty principle, as suggested by Suzuki and Seeger.³ Only some special techniques of electron wave interferometry by Boersch *et al.*⁴ have succeeded in detection of the fluxon existence in a superconducting hollow cylinder without microscopic site determination.

By introducing an electron-holographic technique, on the other hand, we have recently succeeded to overcome the measurement limitation for simultaneously obtaining

high spatial resolution and magnetic-flux sensitivity.⁵ Singly quantized fluxes emerging on the surface of superconducting lead film has been directly imaged in the form of magnetic-flux lines. The present paper reports the detailed analysis on the internal-field distributions around the fluxon center by combining the digital-phase-analysis method⁶ with electron holography. This method allows a numerical measurement of the phase distribution of electron waves by the techniques of digital data processing.⁷ A decomposition of the magnetic-field-vector components from the electron phase distribution has become possible by utilizing the axisymmetry of the fluxon-field distributions. Then a direct comparison between the experimental analysis and the results of theoretical calculation is available. We have numerically calculated the internal-field distribution around the fluxon center in terms of the Ginzburg-Landau (GL) equations, using some models such as the Clem model.⁸ In consequence, an overall agreement was found between the experimental and calculated results.

We also observed structure changes in the magnetic-flux distributions of thin lead films, as a function of their thickness. Our results on the structural transition from the type-I to the type-II-state behaviors of lead films were consistent with those of earlier works.⁹⁻¹⁴ Fluxon pairs consisting of two antiparallel fluxons were also observed in $0.2\text{-}\mu\text{m}$ -thick lead films, which may correspond to the ones suggested in Kosterlitz-Thouless theory.¹⁵

In Sec. II we briefly review the earlier works on the magnetic-flux structures of thin films of type-I superconducting materials, and the experimental techniques for their investigations. Section III is devoted to describing our experimental details and analysis methods supplemented with some mathematical expressions. In Sec. IV, we calculate the internal-field distributions of quantized

fluxes penetrating through a superconductor by numerically solving the GL equations using some models. In particular, the flux spread near the surface of the superconductor is evaluated for a comparison with experiment. Experimental results are shown in Sec. V, and compared with the calculated results in Sec. VI, and finally summarized in Sec. VII.

II. BACKGROUNDS

It is appropriate for the purpose of electron-holographic observation to select a superconducting material of the low value of the GL parameter κ , because the fluxons in such a material are so fine that the flux density is high enough to be detectable. From this point of view, we selected the material lead, of which pure thin films could be simply prepared. The type-I superconductor such as lead enters the intermediate state under the magnetic field between $(1-D)H_c$ and H_c (H_c is the critical field; D is the demagnetization factor). In this state, the macroscopic normal regions (N), through which magnetic fluxes penetrate, appear in the superconducting phase (S). When the thickness of the specimen along the external field becomes thinner, the N/S distribution structure changes in the way that the N region is divided into smaller dimension of normal spots. The variation is based on the change of the thermodynamical free energy which is composed of the N/S interface energy and the nonuniform-magnetic-field energy. Both are in counter-proportional relation with the N/S structure size, whence its equilibrium size is determined from the minimum energy condition for given thickness of the superconductor.

The N/S interface energy can be expressed in terms of the effective GL parameter κ . When the specimen thickness becomes as thin as a critical thickness, the κ value approaches $1/\sqrt{2}$ and the normal spot size is in microscopic scale of the penetration depth λ , containing the magnetic flux quantized in units of Φ_0 . This means that sufficiently thin films of any superconducting materials can go into type-II superconducting states with the mixed state. At the intermediate region of the thickness, the N/S structures and its corresponding magnetic-flux distributions show various kinds of patterns; normal spots (NS) containing macroscopic amounts of fluxes, multiply quantized fluxes (MQF), and singly quantized fluxes (SQF).

Tinkham¹⁶ has pointed out the possibility of the N/S structure changes even for type-I superconducting materials. After this prediction, the magnetic-flux structures in superconducting films have been theoretically studied within GL theory in more detail by Guyon *et al.*,¹⁷ Pearl,¹⁸ Maki,¹⁹ Lasher,²⁰ and Fetter and Hohenberg.²¹ They mainly discussed the stability of each magnetic-flux structure and the critical thickness of the film. According to Lasher,²⁰ as the film thickness increases, the MQF line structures are increasingly more energetically favorable than the SQF structures in the high-field region. In the MQF structure, individual flux bundle with several flux quanta can arrange in the lattice form like Abrikosov's. With further increase of the film thickness, normal-state spots with finite diameters appear

in the superconducting phase and semimacroscopic multiquanta fluxes penetrate therein. This is Goren's normal-spot (NS) model.²² And finally, the laminar structure is most favorable at the sufficiently thick superconductors.

These magnetic-flux structures in thin films of superconducting materials have been experimentally observed in various ways. Direct observations of the SQF static distributions on lead alloy films were performed by Essman and Träuble,^{23,24} and also by Sarma²⁵ with use of the modified Bitter method which had been applied for imaging the domain boundaries in ferromagnetic materials.²⁶ This powerful method has been intensively applied for the investigations of magnetic flux distributions in type-I and -II superconductors of various thicknesses by Barbee,⁹ Rodewald *et al.*,^{10,11,12} and Dolan and Silcox,^{13,14} and many other investigators.²⁷⁻³⁰ The transition from the type-I to type-II-state behavior was also detected by electrical and magnetic measurements.³¹⁻³⁴ Since reports on this particular subject are too numerous to cite comprehensively, the reader should consult Ref. 1 in which is cited additional literature on related work. Earlier results on the magnetic-flux structures in films of type-I superconductors, e.g., lead, may be summarized in a phase diagram at a relatively high temperature T ($T < T_c$), as sketched in Fig. 1. Although the figure is only qualitative and should not be taken strictly, it enables us to explain the conditions under which each investigation is performed, involving the present work. Although most of the earlier works, theoretically and experimentally, were carried out in relatively high-field regions, the present observation covers only very-low-field regions, just above the Meissner phase, due to the ap-

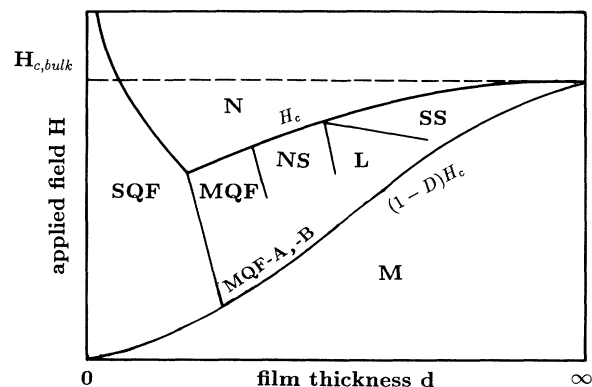


FIG. 1. Schematic phase diagram showing various magnetic-flux structures in a film of a type-I superconducting materials under the magnetic field perpendicular to the film surface. The structures depend on the film thickness and the applied magnetic field. M: Meissner state, N: normal state, SQF: singly quantized flux line structure, MQF: multiply quantized flux line structure, NS: normal spot structure, L: laminar structure, SS: superconducting spot structure. $H_{c,bulk}$ indicates the thermodynamical critical field of a bulk superconductor. D denotes the demagnetization factor. Two types of multiply quantized flux line structures, MQF-A and MQF-B, are found in the present study.

paratus limitation.

In addition to the Bitter method, various kinds of experimental techniques have been employed to observe the magnetic-flux structures in superconductors.^{1,35} They are summarized in Fig. 2 based on their spatial resolution and the sensitivity for magnetic flux. It shows rough estimations of availability of typical experimental methods. The shaded area covers the resolution and sensitivity necessary for observing the mixed state in type-II superconductors. The neutron diffraction method³⁶ allows very quantitative analysis on the flux structures, only when the flux is well periodically distributed. Electron microscopic observations such as shadow electron microscopy,³⁷ electron interferometry,⁴ and out-of-focus electron microscopy,³⁸ have not yet obtained enough spatial resolution and flux sensitivity at the same time. As suggested by Suzuki and Seeger,³ in particular, it is almost impossible to observe the internal field distribution of a single fluxon by out-of-focus electron microscopy because of the uncertainty principle. Recent observation using scanning tunneling microscopy³⁹ reveals a flux-line lattice, which, however, does not probe the magnetic flux itself, but rather the electronic-state changes near the fluxon center at the surface.

Electron holography,⁵ on the other hand, enables one to directly observe individual fluxons quantitatively with high spatial resolution and analyze the internal-field distribution of an individual fluxon, even though the fluxes are themselves not periodically distributed. This method has another advantage in dynamical observation of fluxons. Several investigators tried to observe the movement of the magnetic fluxes in, for instance, lead foils with transport current by means of the Bitter method²⁴ and the shadow electron microscopy.⁴⁰ They have not yet, however, attained satisfactory results, because the former technique is lacking in time resolution and the latter is poor in spatial resolution. In contrast to those tech-

niques, electron holography has sufficiently high temporal and spatial resolution to allow observation of SQF movements. In this paper, though, we focus our attention on static observations of fluxons.

Electron holography was invented by Gabor⁴¹ in order to improve the resolution of electron microscopes. In spite of unsuccessful advances in his original idea, however, an alternate form of the application of electron holography has been successfully developed.⁴² Direct observation of very weak magnetic fields with angstrom resolution has been realized. The principle underlying electron-holographic observation is the Aharonov-Bohm effect.⁴³ The phase of electron waves is affected by magnetic fields, or more strictly speaking, by the magnetic vector potential because the waves carry electric charge.⁴⁴ So we can directly observe the magnetic fields by electron holography which allows an explicit measurement of the phase distribution of the electron wave functions. This fact differentiates electron holography from laser holography in which no magnetic information can be deduced for charge-neutral photons. We have analyzed the detailed magnetic structures of thin films, fine particles, and magnetic recording materials.⁴² The magnetic field distributions are revealed in the form of magnetic flux lines in electron holography micrographs (interference micrographs). Since each line in the micrograph corresponds to a definite amount of magnetic flux h/ne (h is Planck's constant, e is the electric charge of an electron, and n is an integer up to about 100), we can quantitatively analyze the field just by counting the number of the lines. In this paper, furthermore, a more quantitative field analysis is shown by introducing the digital-phase-analysis method.

III. EXPERIMENTAL PROCEDURES AND ANALYSIS METHOD

A. Sample preparation

Superconducting lead film of thickness ranging from $0.1 \mu\text{m}$ to several μm were fabricated by vacuum deposition on one side of a tungsten wire of $30 \mu\text{m}$ diameter at room temperature. We have chosen the film thicknesses according to the earlier works which report that the transition of the magnetic-flux structures from the type-I- to the type-II-state takes place in this range of the thickness.^{14,31} The tungsten wire surface was made clean and smooth in advance by direct current heating up to 2300 K in vacuum. The sample is shown in Fig. 3. The lead film was made up of grains of single crystals, so that special attention was paid to preparation of films almost totally free from surface roughness, pinholes, and cracks at grain boundaries. The critical temperature of the lead films was measured to be 7.2 K, and the residual resistance ratio R_R , $\rho_{300 \text{ K}}/\rho_{7.5 \text{ K}} = 50-80$ for $0.2\text{-}\mu\text{m}$ -thick films and better for thicker films. The quality of the prepared films were recognized in same grade with the specimens in other studies^{14,31} because of the similar R_R values.

The R_R value, a measure of the disorder in the film structure, always corresponds to the effective mean free path,⁴⁵

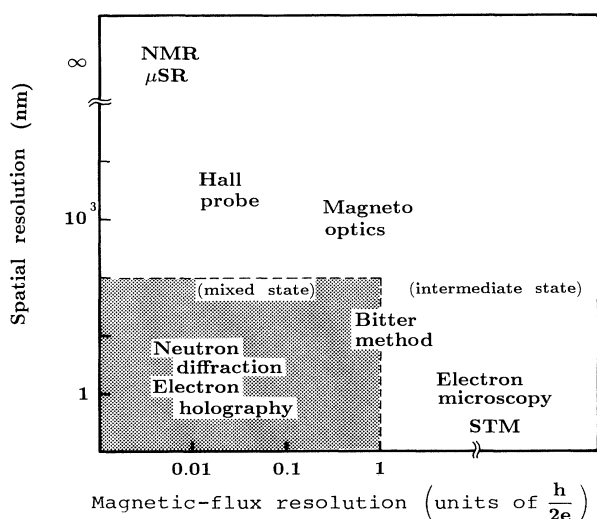


FIG. 2. Typical experimental methods to observe the flux structures in superconductors. They are roughly classified in terms of their spatial resolutions and magnetic-flux resolutions.

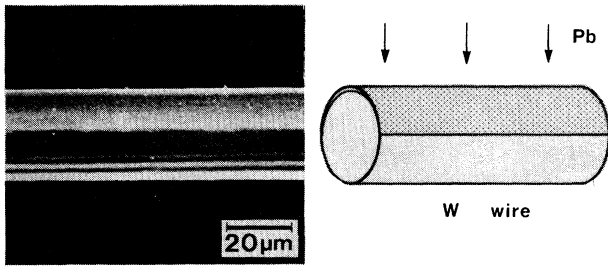


FIG. 3. Scanning electron micrograph of the observation sample. The lead film was deposited on one side of a tungsten wire of $30\ \mu\text{m}$ diameter.

$$l = (R_R - 1) \frac{\rho l}{\rho_{300\text{ K}}}, \quad (1)$$

where the values of ρl and $\rho_{300\text{ K}}$ are obtained from the literature;⁴⁶ $\rho l = 1.5 \times 10^{-11}\ \Omega\text{cm}^2$, $\rho_{300\text{ K}} = 21\ \mu\Omega\text{cm}$. From the values of R_R for our lead films; $R_R = 50\text{--}80$ for the $0.2\text{-}\mu\text{m}$ -thick films, we obtain $l = 360\text{--}560\text{ nm}$.

In the case of sufficiently thin films, on the other hand, the effective mean free path is limited primarily from diffuse reflection of the electrons at the sample surfaces. According to the Fuch's classical theory of the size effect,⁴⁷

$$\frac{1}{l} = \frac{1}{l_\infty} + \frac{3}{8d}, \quad \frac{l}{l_\infty} > 0.1, \quad (2)$$

where l_∞ is the mean free path of a bulk specimen of the same purity and defect content, and d is the film thickness. For the film of $d = 0.2\ \mu\text{m}$, using the value of l above obtained, l_∞ should be longer than $1.1\ \mu\text{m}$ estimated from Eq. (2). This implies that our lead films had enough high quality and purity so that the mean free path is not limited by the impurity and defect scatterings, but primarily by the film thickness.

The wire was fixed on a sample holder with indium-layer thermal contact. In our electron holography microscope (Fig. 4), the lead film was cooled down to be superconducting with fluxons under the magnetic field perpendicular to the film surface. Because the electron beam could not transmit through the film, we could only observe the fluxons spreading out into vacuum outside the film surface, not the fluxons in the film. So we had to catch the root of the fluxon just above the film surface in order to investigate the internal field distribution of the fluxon inside the film. For this reason the film was curved to ensure the fluxons exit at the extreme edge of the sample shadow.

But the observed fluxons were not necessarily located on the extreme edge of the sample shadow. In fact, fluxons with different root diameters were observed even on the same sample. Therefore, we cannot measure the intrinsic fluxon diameters with fluxons of broader roots which do not stand on the extreme edge and are probably shadowed by the edge. Since, however, it is considered that the fluxons with the finest roots among the large number of observed fluxons really exit at the extreme

edge of the sample shadow, they were used for the analysis of the inner field distribution around the fluxon center.

B. Electron-holography microscope

Our microscope was an H-800 type Hitachi transmission electron microscope devised for electron holography with a cold field-emission type electron gun and a Mollenstedt-type electron biprism.⁴⁸ Its operating voltage was 150 kV. It also had a sample cooling stage and electromagnet pairs to apply the magnetic field perpendicular to the lead film.

The sample-cooling stage depicted in Fig. 5 was set in the sample chamber of the microscope column and thermally connected to a liquid helium and nitrogen container which was set outside the column. The sample holder (SH) was introduced from the sample exchange chamber (EC) through the gate valve (GT) and rapidly cooled down from room temperature by thermal connection with the stage. The sample holder, which can be cooled down to 2.5 K by pumping out the liquid helium container, is surrounded with two shells for thermal radiation shielding. The intermediate shell (HJ1) was cooled down to 5 K with liquid helium and the outer (NJ) was 100 K with liquid nitrogen. The sample temperature could be reversibly set at any points between 2.5 and 20

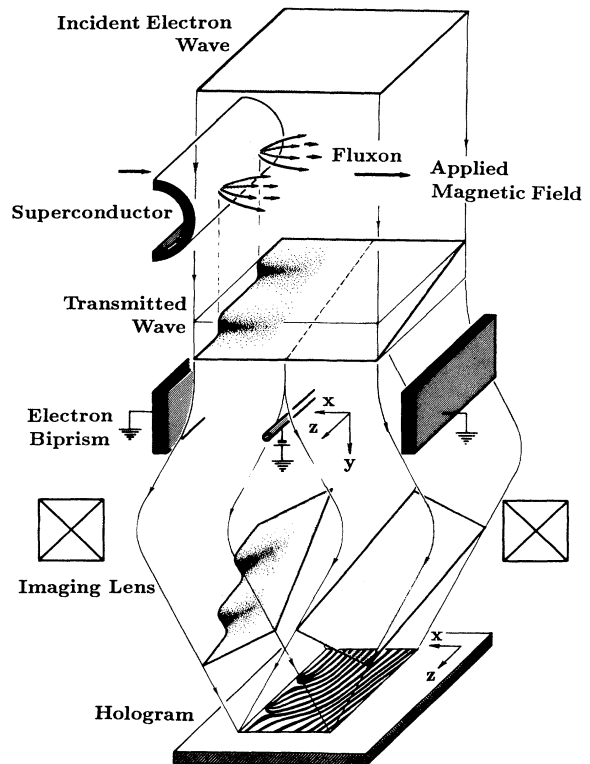


FIG. 4. The electron wave propagation in the electron holography microscope. The wavefront is deformed by the fluxons and divided into two parts, an object wave and a reference wave, by an electron biprism to form a hologram.

K with a heater attached to the stage. Annealed silver flexible foils of $30\ \mu\text{m}$ thickness (AF) were used for the thermal connection of the sample to the refrigerant container, and at the same time, for the absorption of the external mechanical vibrations.

The first electromagnet pair (EM1) produces the transverse magnetic field up to 35 Oe to create the fluxons in the lead film. Since the field, however, deflects the electron beam (EB), we need the second (EM2) and third electromagnet pairs (EM3) to correct the beam path for microscopic observation. The excitation of the latter two electromagnets are adjusted according to the first magnetic field strength. In this way it became possible to carry out the in-field cooling and the in-field observation, of which temperature and magnetic field ranges were 2.5–20 K and -35 –35 Oe, respectively.

The propagation of electron waves in the microscope is illustrated in Fig. 4. The illuminating electron wave, emitted from the field emission tip, is regarded as a plane wave $\psi_{\text{inc}} = \exp\{ik_0y\}$ (the wave propagates along the y axis and k_0 is the wave number of the electron). Transmitting through the sample region, the wave front is deformed by the magnetic field; the localized field of a fluxon causes steep phase change, although the wave front passing far from the lead film is only inclined smoothly because of a uniform field. By electron biprism action, the transmitted wave is divided into two parts, su-

perimposed, and interfere with each other. Interference fringes were recorded on a hologram. One of the divided waves, passed near the lead film surface, becomes an object wave which contains the information on the fluxons. It is expressed as

$$\psi_{\text{obj}} = \exp\{ik_1y + ik_2x + i\phi(x,z)\}, \quad (3)$$

where $\phi(x,z)$ is the phase shift caused by the fluxons, and the phase factor $\exp\{ik_2x\}$ denotes the beam deflection in the x direction by the electron biprism, and $k_0^2 = k_1^2 + k_2^2$. Another wave, passed through the far distant region, $\sim 6\ \mu\text{m}$ from the investigated lead film surface at the specimen plane, acts as a reference wave. It is expressed as a plane wave

$$\psi_{\text{ref}} = \exp\{ik_1y - ik_2x\}, \quad (4)$$

because the beam deflection by the biprism occurs in the symmetrically opposite ($-x$) direction with the object wave Eq. (3). The phase distribution of the object wave $\phi(x,z)$ is thus recorded in the form of interference fringe distributions, an off-axis hologram $I_{\text{hol}}(x,z)$;

$$I_{\text{hol}}(x,z) = |\psi_{\text{obj}} + \psi_{\text{ref}}|^2 \sim 1 + \cos \left[\frac{2k_2x}{M} + \phi \left(\frac{x}{M}, \frac{z}{M} \right) \right], \quad (5)$$

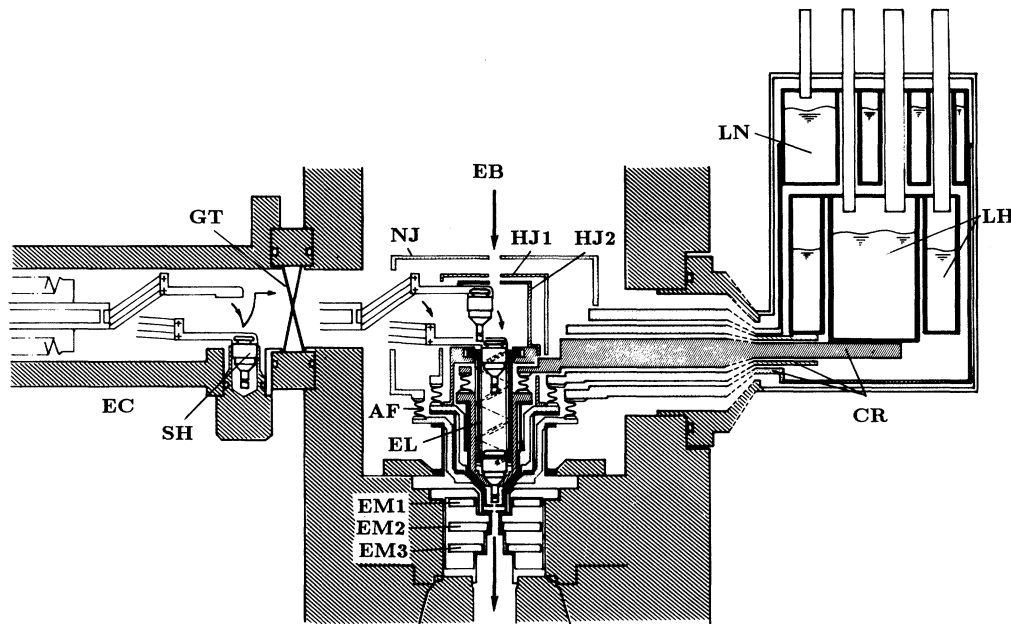


FIG. 5. The sample cooling stage and the electromagnet pairs equipped in the sample chamber of the electron microscope column. The sample holder (SH) is introduced from the exchange chamber (EC) through the gate valve (GT) into the column. The holder is set at the observation position by the elevator (EL) and thermally connected to the cooling stage. The stage is connected through a Cu rod (CR) to a liquid helium (LH) and nitrogen (LN) containers set outside the column. The stage and container are composed of three shells; the outer shell (NJ) is cooled down to 100 K by the liquid nitrogen, the intermediate shells (HJ1) is 5 K by the liquid helium, and the inner shell (HJ2), which contacts to the sample holder, is 2.5 K by pumping the inner liquid helium container. Thin flexible Ag foils (AF) thermally connect the sample and the refrigerant container, and at the same time, absorb mechanical vibrations. The first electromagnet pair (EM1) apply the magnetic field perpendicular to the sample lead film. The second (EM2) and the third (EM3) electromagnet pairs correct the electron beam (EB) path deflected by EM1 for microscopic observation.

where $\pi M/k_2$ is the carrier fringe spacing in the hologram and M is the magnification of the image. For simplicity we have neglected here the uniform phase shift by the uniform applied magnetic field.

Strictly speaking, the reference wave is not a plane wave because the magnetic field modulation by the fluxons virtually extends, decaying exponentially from the film surface, into the reference wave area at the specimen plane. Since, however, the phase change caused by the modulation in the reference wave area is estimated to be less than $\pi/200$ which is smaller than the experimental precision, the reference wave can be regarded as plane and the phase distribution recorded on the hologram is only the object wave's. Moreover the divergence angle of the illuminating electron beam is $\sim 1 \times 10^{-8}$ rad so that the incident wave is also regarded as a plane wave with $\pi/500$ accuracy.

The sample image was focused by the intermediate lens, because the objective lens was switched off to prevent the extra field applying the sample. An image hologram with magnification M of 1500–2000 was obtained by applying a negative voltage (~ -20 V) to the central thin wire of the electron biprism. The holograms were recorded on Kodak 4489 electron microscope films. The carrier fringes were set to be parallel to the lead film edge shadow, or perpendicular to the fluxons, in the hologram. The hologram width and its carrier fringe spacing were set to be 4–10 mm and 60–100 μm on the film, or 4–6 μm and 30–60 nm at the specimen plane, respectively.

C. Optical reconstruction with digital-phase-analysis method

Although the phase distribution $\phi(x, z)$ of the electron wave passed through the fluxons is recorded on the holo-

gram as Eq. (5), we cannot read out the phase information directly from it, because the interference fringes in the hologram are very fine and are not the contour phase lines. So we utilized a laser interferometer for the optical reconstruction to visualize the phase distribution as contour phase lines. After developing and fixing the hologram, it was set in a Twyman-Green-type laser interferometer as shown in Fig. 6. The He-Ne laser beam is divided into two beams by a beam splitter, and after reflected by the mirrors *A* and *B*, each beam irradiates the hologram. The illuminating laser beams are plane waves. In addition to the transmitted waves which are also plane waves, a set of the \pm first-order diffracted waves emerge from each illuminating beam, because the hologram with the carrier fringes acts as a grating. The diffracted waves have the phase information recorded on the hologram. Only the +first-order diffracted wave from the beam reflected by the mirror *A*

$$\psi_{+1} = \exp\{iK_1 y + i2k_2 x + i\phi(x, z)\} \quad (6)$$

and the $-$ first-order one from another beam reflected by the mirror *B*

$$\psi_{-1} = \exp\{iK_1 y - i2k_2 x - i\phi(x, z)\} \quad (7)$$

were selected. Here $K_0 \equiv \{K_1^2 + (2k_2)^2\}^{1/2}$ corresponds to the wave number of the laser beam and the magnification M in Eq. (5) was omitted for simplicity. They were then adjusted to propagate in the *y* direction by inclining the mirrors,

$$\psi_{+1} = \exp\{iK_0 y + i\phi(x, z)\}, \quad (8)$$

$$\psi_{-1} = \exp\{iK_0 y - i\phi(x, z)\}, \quad (9)$$

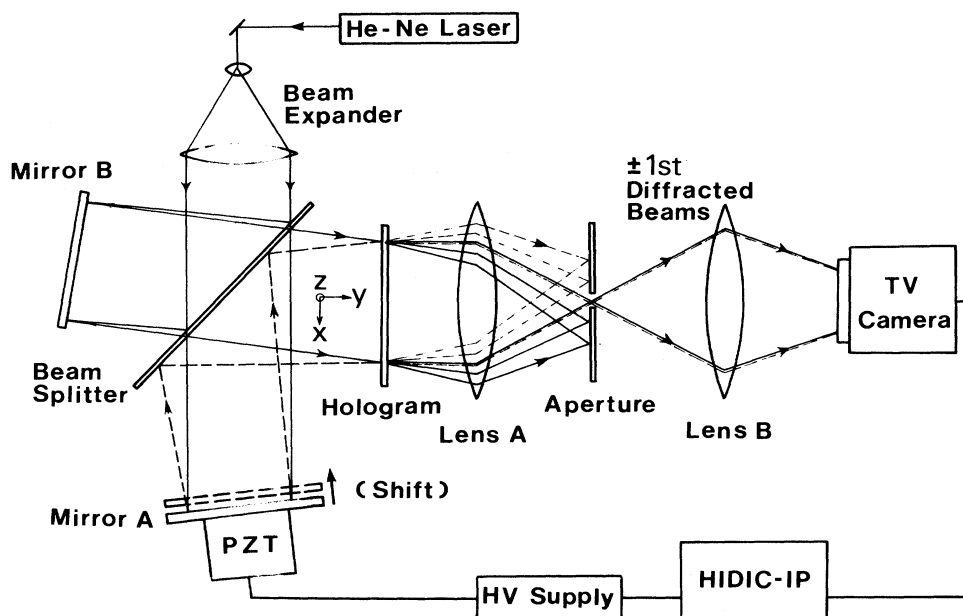


FIG. 6. Laser interferometer for the optical reconstruction with the fringe scanning interferometry. The interference micrographs are stored in a Hitachi image processing computer HIDIC-IP which also control a high voltage (HV) supply to derive a piezoelectric transducer (PZT).

and were made to interfere with each other to form an interference micrograph $I(x, z)$;

$$I(x, z) = |\psi_{+1} + \psi_{-1}|^2 \sim 1 + \cos\{2\phi(x, z)\}. \quad (10)$$

The carrier fringes are in this way removed, and the interference fringes in this image become contour phase lines of π interval. This is an interference micrograph.

The fringe intensity distribution in the real micrograph is, however, expressed as

$$I(x, z) = a(x, z) + b(x, z)\cos\{2\phi(x, z)\}, \quad (11)$$

instead of Eq. (10), because the average fringe intensity $a(x, z)$ and the fringe contrast $b(x, z)$ are not constant over the image due to the nonuniformity of the illuminating laser beams, nonlinearity of the photographic film, the speckle noise, and others. Although the interference micrograph Eq. (11) directly shows the phase distribution $\phi(x, z)$ in units of π , moreover, we cannot measure the phase distribution with the phase resolution higher than π . In other words, the phase information between the neighboring fringes in the interference micrograph cannot be displayed. To read out the subfringe information from the hologram with higher accuracy, then, we have adopted a digital phase analysis method called "fringe scanning interferometry"⁴⁹ which utilizes the digital image-processing technique with a computer. This method allows the numerical measurement of the phase distribution of the wave reconstructed from the hologram and improve the phase measurement precision up to $\sim \pi/50$.

Stepwise movement of the mirror A of the interferometer of Fig. 6, driven by a piezoelectric transducer (PZT), causes a fringe shift in the interference micrograph Eq. (11) because the relative phase difference between ψ_+ and ψ_- changes with the mirror movement. Images at four different mirror positions, of which position interval is $\lambda/8$ (λ is the wavelength of the He-Ne laser beam, 6328 Å),

$$I(x, z; n) = a(x, z) + b(x, z)\cos\left[2\phi(x, z) + \frac{2\pi n}{4}\right] \quad (12)$$

($n=0-3$) were synchronously stored through a TV camera (512×512 pixels) in a HIDIC-IP Hitachi image-processing minicomputer. A pixel corresponds to a ~ 8 -nm-square on the specimen plane. The irradiance at each pixel in the interference micrograph goes through one cycle of periodic variation with the mirror movement. The computer determines a best-fit sinusoidal function for the irradiance versus the amount of phase shift at each pixel in the micrograph. The phase of the best-fit function is a direct measure of the investigated wave front. According to the fringe-scanning phase-detection principle,⁴⁹ summations with sinusoidal weights

$$\begin{aligned} C(x, z) &= \sum_{n=0}^3 I(x, z; n) \cos\left[\frac{2\pi n}{4}\right] \\ &= I(x, z; 0) - I(x, z; 2), \end{aligned} \quad (13)$$

$$\begin{aligned} S(x, z) &= \sum_{n=0}^3 I(x, z; n) \sin\left[\frac{2\pi n}{4}\right] \\ &= I(x, z; 1) - I(x, z; 3), \end{aligned} \quad (14)$$

are calculated from the four images Eq. (12) to extract the sinusoidal parts of the intensity variation. This method enables one to separate the phase information $\phi(x, z)$ from the fringe average $a(x, z)$ and contrast $b(x, z)$ of the interference pattern. The phase of the pixel is then given by

$$\begin{aligned} \phi(x, z) &= \arctan \frac{S(x, z)}{C(x, z)} \\ &= \arctan \frac{I(x, z; 1) - I(x, z; 3)}{I(x, z; 0) - I(x, z; 2)}. \end{aligned} \quad (15)$$

The calculated arctangent values are wrapped between $\pm\pi$. The unwrapped phase value gives the correct shape corresponding to the phase profile. By performing the above calculation all over the pixels in the image, the electron wave front is numerically reconstructed.

D. Electron phase and magnetic field

We now review the relation between the phase of the electron wave and the magnetic field for preparing the analysis of the fluxon fields. The Aharonov-Bohm effect⁴³ predicts that the magnetic flux Φ causes the phase shift $\Delta\phi$ between the electron wave front elements passing through either side of the flux (Fig. 7):

$$\Delta\phi = 2\pi \frac{\Phi}{(h/e)}. \quad (16)$$

A single flux quantum $h/2e$ ($=2.07 \times 10^{-15}$ Wb), therefore, causes the phase shift of π . The contour phase lines

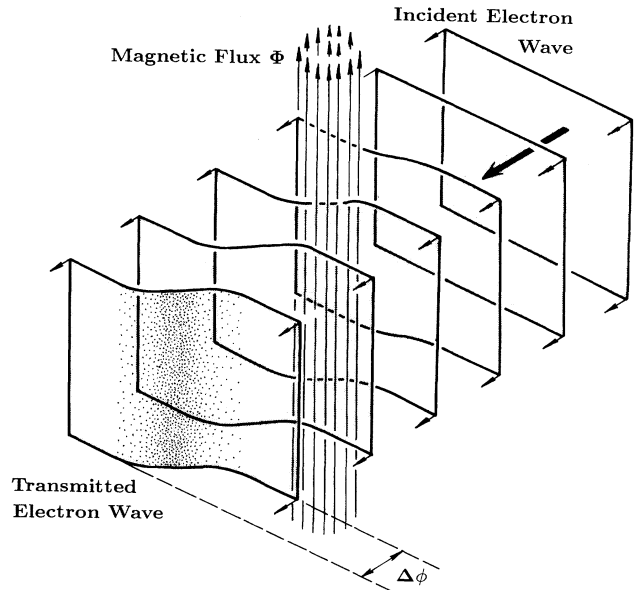


FIG. 7. The Aharonov-Bohm effect predicts that the phase shift $\Delta\phi$ of the electron wave transmitted through the magnetic flux Φ is related by $\Delta\phi = 2\pi\Phi/(h/e)$.

in the interference micrograph drawn in units of π in the way previously mentioned directly correspond to the magnetic flux lines in units of $h/2e$.

It is not only the amount of the flux, but also the internal field distribution of the flux that we can measure from the curvature of the transmitted wave front. We set up a coordinate system as shown in Fig. 8 to give some mathematical expressions. The z axis is the core axis of an isolated fluxon, and the region of $z \leq 0$ is occupied by a semi-infinite superconductor. The region of $z \geq 0$ is vacuum and the surface of the superconductor is the plane $z=0$. The incident electron wave $\psi_{\text{inc}} = \exp\{ik_0y\}$ comes from $y = -\infty$ along the y axis. Its wave front is parallel with the (xz) plane and infinitely spreads in the vacuum $z \geq 0$. Transmitting through the fluxon, the wave gets the phase shift $\phi(x, z)$ which is expressed by a line integral of the vector potential \mathbf{A} along the path of the wave front element of interest:

$$\phi(x, z) = -\frac{e}{\hbar} \int_{\text{path1}} \mathbf{A} \cdot d\mathbf{s} . \quad (17)$$

Taking into the spatial resolution of our observation, we can neglect the deflection of the path by the fluxon field. In fact, its deflection angle is $\sim 10^{-5}$ rad and the decrease of the spatial resolution by this effect in an in-focused hologram is estimated 0.001 nm. So path 1 is regarded as a straight line passing through the point $(x, 0, z)$ and parallel to the y axis. In the same way we obtain

$$\phi(x + dx, z) = -\frac{e}{\hbar} \int_{\text{path2}} \mathbf{A} \cdot d\mathbf{s} \quad (18)$$

for the neighboring wave front element. Subtracting Eq. (17) from Eq. (18) we get

$$\begin{aligned} \phi(x + dx, z) - \phi(x, z) &= \frac{\partial \phi(x, z)}{\partial x} dx \\ &= -\frac{e}{\hbar} \left[\int_{\text{path2}} \mathbf{A} \cdot d\mathbf{s} - \int_{\text{path1}} \mathbf{A} \cdot d\mathbf{s} \right] . \end{aligned} \quad (19)$$

We can regard path 1 and path 2 as the same at $y = \pm\infty$, Eq. (19) is rewritten as

$$\frac{\partial \phi(x, z)}{\partial x} dx = -\frac{e}{\hbar} \oint \mathbf{A} \cdot d\mathbf{s} , \quad (20)$$

where the integral is carried out along the closed path determined by paths 1 and 2. According to the Stokes theorem and $\text{rot } \mathbf{A} = \mathbf{B}$ (\mathbf{B} is the magnetic flux density vector),

$$\frac{\partial \phi(x, z)}{\partial x} dx = -\frac{e}{\hbar} \int \mathbf{B} \cdot d\mathbf{S} , \quad (21)$$

where the surface integral is performed over the surface bordered by the closed path. Since the surface element $d\mathbf{S}$ points to the positive direction of the z axis and $|d\mathbf{S}| = dx \cdot dy$,

$$\frac{\partial \phi(x, z)}{\partial x} dx = -\frac{e}{\hbar} dx \int_{-\infty}^{\infty} dy B_z(x, y, z) , \quad (22)$$

and consequently

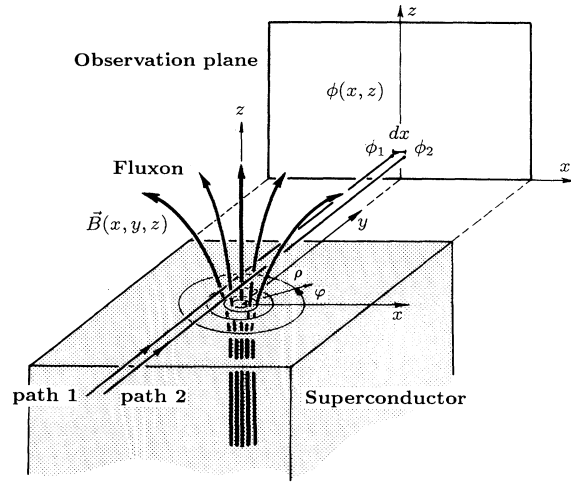


FIG. 8. Coordinate system for analyzing the internal field distribution around a fluxon center from the measured phase distribution of the passed electron wave.

$$\frac{\partial \phi(x, z)}{\partial x} = -\frac{e}{\hbar} \int_{-\infty}^{\infty} dy B_z(x, y, z) . \quad (23)$$

In the same way we get

$$\frac{\partial \phi(x, z)}{\partial z} = \frac{e}{\hbar} \int_{-\infty}^{\infty} dy B_x(x, y, z) \quad (24)$$

for the field-vector component parallel to the superconductor surface. In this way, by differentiating the measured phase distribution of the electron wave, we obtain a two-dimensional projection of the three-dimensional magnetic field distribution along the direction of view. Data processing of the numerically measured phase is possible with an image processing computer.

On the next step we calculate the field vector components B_z, B_x (or B_ρ) themselves from their projections Eqs. (23) and (24). Since the magnetic field distribution \mathbf{B} of the fluxon and the persistent current \mathbf{j} circulating around the fluxon are axisymmetric with respect to the z axis, we introduce the cylindrical coordinate (ρ, φ, z) (Fig. 8). \mathbf{j} has only the φ component only in the superconductor. But \mathbf{B} has the z and ρ components near the superconductor surface and in vacuum, although it has only the z component in the sufficiently inner bulk region of the superconductor.

We now employ the same algorithm as the reconstruction of the three-dimensional structure from the electron microscope image using the Fourier transform.⁵⁰ We at first calculate the Fourier transform $F(X, z)$ of Eq. (23) with respect to x :

$$\begin{aligned} F(X, z) &= \int_{-\infty}^{\infty} dx \frac{\partial \phi(x, z)}{\partial x} e^{2\pi i x X} \\ &= -\frac{e}{\hbar} \int_{-\infty}^{\infty} dx \int_{-\infty}^{\infty} dy B_z(x, y, z) e^{2\pi i x X} . \end{aligned} \quad (25)$$

Transforming into the cylindrical coordinate, $B_z(x, y, z) = B_z(\rho, z)$ (B_z is independent of φ coordinate)

$$F(X, z) = -\frac{e}{\hbar} \int_0^{2\pi} d\varphi \int_0^\infty d\rho \rho B_z(\rho, z) e^{2\pi i \rho X \cos\varphi}. \quad (26)$$

Taking into account the definition of the n th order Bessel function

$$J_n(x) = \frac{1}{2\pi i^n} \int_0^{2\pi} d\varphi e^{i(x \cos\varphi + n\varphi)}, \quad (27)$$

Equation (26) is rewritten as

$$F(X, z) = -\frac{2\pi e}{\hbar} \int_0^\infty d\rho \rho B_z(\rho, z) J_0(2\pi\rho X). \quad (28)$$

After multiplying $X \cdot J_0(2\pi t X)$ to both sides of Eq. (28), and integrating with X we get

$$\int_0^\infty dX X F(X, z) J_0(2\pi t X) = -\frac{2\pi e}{\hbar} \int_0^\infty d\rho \int_0^\infty dX \rho X B_z(\rho, z) J_0(2\pi\rho X) J_0(2\pi t X). \quad (29)$$

By replacing $\eta = 2\pi X$, the right-hand side of Eq. (29) is

$$-\frac{e}{2\pi\hbar} \int_0^\infty d\rho \int_0^\infty d\eta \rho \eta B_z(\rho, z) J_0(\rho\eta) J_0(t\eta). \quad (30)$$

Using the identity for the Fourier-Bessel integral theorem for an arbitrary function $f(t)$,

$$f(t) = \int_0^\infty d\rho \int_0^\infty d\eta \rho \eta f(\rho) J_n(\rho\eta) J_n(t\eta), \quad (31)$$

Equation (30) is equivalent to $-(e/2\pi\hbar)B_z(t, z)$. Consequently Eq. (29) is reduced to

$$B_z(\rho, z) = -\frac{2\pi\hbar}{e} \int_0^\infty dX X F(X, z) J_0(2\pi\rho X). \quad (32)$$

In the same way, the ρ component is given as described in the Appendix by

$$B_\rho(\rho, z) = \frac{2\pi\hbar}{ie} \int_0^\infty dX X S(X, z) J_1(2\pi\rho X), \quad (33)$$

where

$$S(X, z) \equiv \int_{-\infty}^\infty dx \frac{\partial\phi(x, z)}{\partial z} e^{2\pi i x X}. \quad (34)$$

By differentiating the measured phase distribution of the electron wave and taking their Fourier transforms, each component of the field vector \mathbf{B} can be in this way calculated. In Sec. V we actually calculated the components from the phase data measured by the fringe scanning interferometry, and then the results are compared with the field distribution calculated from the Ginzburg-Landau equations.

IV. MODEL CALCULATIONS OF INTERNAL FIELD DISTRIBUTIONS

In this section we numerically calculate the internal field distributions of quantized magnetic fluxes near the surface of a superconductor. The magnetic-flux distribution around the fluxon center in the superconductor has been qualitatively described by the London model⁵¹ and semiquantitatively by the Clem model.⁸ For quantitative discussions for the field distribution, the GL equations, or more strictly speaking, the Eilenberger equations⁵² derived from the Gor'kov equation, should be solved. But it needs a huge numerical calculation with a high-speed

computer.

Since we could not observe the fluxons *in* the superconductor, but only the fluxons appearing *on* the superconductor surface as mentioned so far, the comparison with theories is not straightforward. For the flux begins to spread even below the superconductor surface so that the field distribution around the core axis differs from that in the inner bulk. Then we numerically solved the GL equations in the superconductor and the Maxwell equations in vacuum in order to correctly evaluate the flux spreading near the surface. Although our experiments were carried out in the range of low magnetic fields and low temperatures, in which the GL theory is not applicable, we start from the equations often used for phenomenological understanding. Since, however, the GL equations,

$$-\frac{\hbar^2}{2m} \left[\nabla - \frac{2ie}{\hbar} \mathbf{A} \right]^2 \Psi = \alpha \Psi - \beta |\Psi|^2 \Psi, \quad (35)$$

$$\frac{1}{\mu_0} \text{rot rot } \mathbf{A} = n_s \left[\frac{\hbar e}{2mi} (\Psi^* \nabla \Psi - \nabla \Psi^* \Psi) - \frac{2e^2}{m} |\Psi|^2 \mathbf{A} \right], \quad (36)$$

where $\Psi(\mathbf{r})$ is the order parameter, $\mathbf{A}(\mathbf{r})$ the vector potential, μ_0 the permeability of the vacuum, n_s the number density of the Cooper pairs, α and β are the coefficients calculated from the BCS theory, are nonlinear for the unknown functions $\Psi(\mathbf{r})$ and $\mathbf{A}(\mathbf{r})$, we cannot easily solve them. So we assumed some functions for $\Psi(\mathbf{r})$ and solved Eq. (36) only for $\mathbf{A}(\mathbf{r})$. Once the vector potential is obtained we can calculate the flux density $\mathbf{B}(\mathbf{r})$ and the persistent current density $\mathbf{j}(\mathbf{r})$ circulating around the flux:

$$\mathbf{B}(\mathbf{r}) = \text{rot } \mathbf{A}(\mathbf{r}), \quad (37)$$

$$\mathbf{j}(\mathbf{r}) = \frac{1}{\mu_0} \text{rot rot } \mathbf{A}(\mathbf{r}). \quad (38)$$

Using the coordinate system shown in Fig. 8, the fluxon near the surface is described by

$$\begin{aligned}
\Psi(\rho, \varphi, z) &= |\Psi(\rho, z)| e^{-i\varphi}, \\
\mathbf{A}(\rho, \varphi, z) &= A_\varphi(\rho, z) \hat{\varphi}, \\
\mathbf{B}(\rho, \varphi, z) &= B_\rho(\rho, z) \hat{\rho} + B_z(\rho, z) \hat{z}, \\
\mathbf{j}(\rho, \varphi, z) &= j_\varphi(\rho, z) \hat{\varphi},
\end{aligned} \tag{39}$$

where $\hat{\rho}$, $\hat{\varphi}$, and \hat{z} are the unit vectors for the respective directions. Equation (36) then has only the φ component:

$$\begin{aligned}
\frac{\partial^2 A_\varphi(\rho, z)}{\partial z^2} + \frac{\partial}{\partial \rho} \left[\frac{1}{\rho} \frac{\partial}{\partial \rho} [\rho A_\varphi(\rho, z)] \right] \\
- \frac{1}{\lambda^2} \left[A_\varphi(\rho, z) - \frac{\Phi_0}{2\pi\rho} \right] |\Psi(\rho, \varphi, z)|^2 = 0, \tag{40}
\end{aligned}$$

where the magnetic-flux penetration depth $\lambda = (m/2e^2\mu_0 n_s)^{1/2}$ and the magnetic-flux quantum $\Phi_0 = h/2e$. And then, from Eqs. (37) and (38),

$$B_\rho(\rho, z) = -\frac{\partial A_\varphi(\rho, z)}{\partial z}, \tag{41}$$

$$B_z(\rho, z) = \frac{1}{\rho} \frac{\partial}{\partial \rho} \{ \rho A_\varphi(\rho, z) \}, \tag{42}$$

$$\begin{aligned}
j_\varphi(\rho, z) &= \frac{1}{\mu_0} \left[\frac{\partial B_\rho(\rho, z)}{\partial z} - \frac{\partial B_z(\rho, z)}{\partial \rho} \right] \\
&= -\frac{1}{\lambda^2} \left[A_\varphi(\rho, z) - \frac{\Phi_0}{2\pi\rho} \right] |\Psi(\rho, \varphi, z)|^2. \tag{43}
\end{aligned}$$

For the SQF line we adopt the Clem model⁸ for the order parameter:

$$\Psi_1(\rho, \varphi, z) = \begin{cases} \frac{\rho}{(\rho^2 + \xi^2)^{1/2}} e^{-i\varphi} & (z \leq 0), \\ 0 & (z > 0), \end{cases} \tag{44}$$

where ξ is the coherence length which approximately corresponds to the radius of the fluxon. We assume the z independence of the order parameter near the superconductor surface. Equation (40) then becomes the Maxwell equation in vacuum $z > 0$. Equation (40) with Eq. (44) was numerically solved by the finite difference method using the DEQSOL (differential equation solver) program⁵³ with a Hitachi computer HITAC M680H. The area for solving the equation was a square of $\rho = 0-1 \mu\text{m}$, $z = -0.5-0.5 \mu\text{m}$ with 200×200 square meshes (Fig. 9), and the boundary conditions were

$$A_\varphi = 0, \text{ because of the symmetry on } \rho = 0;$$

$$A_\varphi = \frac{\Phi_0}{2\pi\rho}, \text{ implying } B_\rho = 0, \text{ on } \rho = 1 \mu\text{m}; \tag{45}$$

$$A_\varphi = \frac{\Phi_0}{2\pi\lambda^2} \frac{\rho}{400},$$

implying $B_z = \text{const}$, on $z = 0.5 \mu\text{m}$;

$$\frac{\partial A_\varphi}{\partial z} = 0, \text{ implying } B_\rho = 0, \text{ on } z = -0.5 \mu\text{m}.$$

The boundary conditions Eq. (45) should be different between an isolated fluxon and a fluxon in a flux line lattice, but the calculated internal field distribution around the fluxon center near the superconductor surface was almost independent of the boundary conditions and the calculation area size. Our main interest in the analysis of the experimental results lies in the internal field distribution at the flux root just above the superconductor surface.

For numerically solving the GL equation Eq. (40) with the Clem model Eq. (44), we must estimate the characteristic parameters of our lead films, λ and ξ . In the case of superconductors characterized by the local field theory, the weak-field penetration depth $\lambda(T, d)$, which depends on the temperature T and possibly on the film thickness d , is given by⁵⁴

$$\lambda(T, d) = \lambda_L(T) \left[1 + \frac{\xi_0}{l} \right]^{1/2}. \tag{46}$$

Here, $\lambda_L(T)$ is the London penetration depth, ξ_0 is the Pippard coherence distance, and l is an effective mean free path arising from either scattering by impurities or

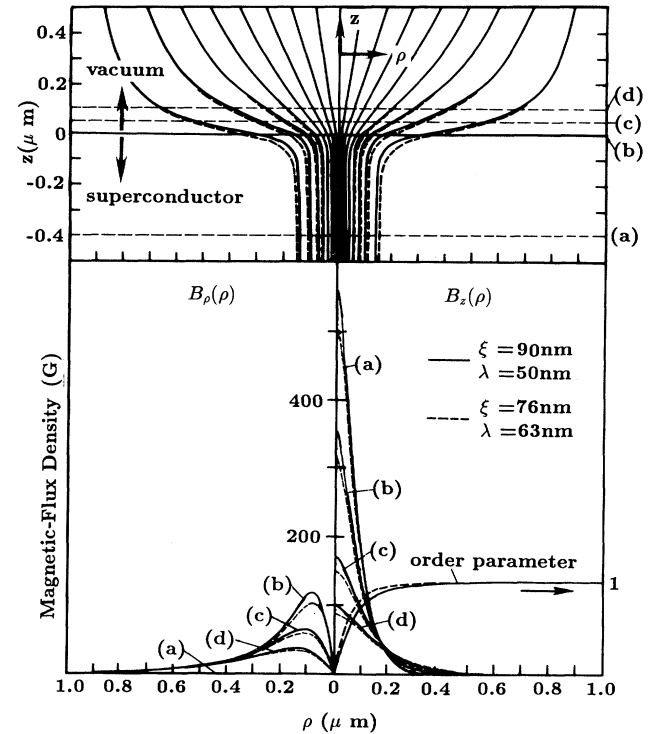


FIG. 9. The magnetic-flux distributions of a fluxon near the superconductor surface, calculated with the DEQSOL program using the Ginzburg-Landau equation Eq. (40) combined with the Clem model equation (44). The curved solid lines are calculated with the parameters, $\xi = 90 \text{ nm}$, $\lambda = 50 \text{ nm}$, and the curved dash lines are with $\xi = 76 \text{ nm}$, $\lambda = 63 \text{ nm}$. The upper figure shows the flux-line distributions. The lower figure shows the profiles of the field distribution along the lines indicated in the upper figure. The field-vector components are separately shown.

the surfaces of the film. Since a real sample, lead, is not, however, recognized to be quite local, Tinkham³¹ has suggested the following modification of Eq. (46) as a suitable extrapolation form for $\lambda(T, d)$;

$$\lambda(T, d) = \lambda(T, \infty) \left[1 + \frac{[\lambda_L(T)]^2 \xi_0}{[\lambda(T, \infty)]^2 l} \right]^{1/2}, \quad (47)$$

where $\lambda(T, \infty)$ is the bulk weak-field penetration depth. We assume the temperature dependence of λ 's by the usual Gorter-Casimir ones, namely, $\lambda(t) = \lambda(0) / (1 - t^4)^{1/2}$, where $t = T/T_c$. Then, Eq. (47) becomes

$$\lambda(T, d) = \frac{\lambda(0, \infty)}{(1 - t^4)^{1/2}} \left[1 + \frac{[\lambda_L(T)]^2 \xi_0}{[\lambda(T, \infty)]^2 l} \right]^{1/2}. \quad (48)$$

Using the values of the effective mean free path l obtained in Sec. III and $[\lambda_L(T)^2 / \lambda(T, \infty)^2] \xi_0 = 69$ nm at $T = 4.2$ K, $\lambda(0, \infty) = 44$ nm,³¹ we get $\lambda(4.2$ K, 200 nm) = 50–52 nm.

In the same way, the GL parameter $\kappa(T, d)$ is given by³¹

$$\kappa(T, d) = \kappa(T, \infty) \left[1 + \frac{[\lambda_L(T)]^2 \xi_0}{[\lambda(T, \infty)]^2 l} \right], \quad (49)$$

where

$$\begin{aligned} \kappa(T, \infty) &= \frac{2\sqrt{2} \pi H_c(T) [\lambda(T, \infty)]^2}{h/2e} \\ &= \frac{2\sqrt{2} \pi H_c(0) [\lambda(0, \infty)]^2}{(1 + t^2) h/2e}. \end{aligned} \quad (50)$$

Here, H_c is the thermodynamical critical field, $H_c(0) = 803$ G, and $h/2e = 2.07 \times 10^{-15}$ Wb, the flux quantum. We obtain, therefore, $\kappa(4.2$ K, 200 nm) = 0.56–0.59, and consequently, from the relation $\xi(T, d) = \lambda(T, d) / \kappa(T, d)$, we get $\xi(4.2$ K, 200 nm) = 88–90 nm. These values of the parameters, λ and ξ , for our lead films are not dissimilar to other reports,^{12,14} in spite of our unusual substrate for the lead deposition. We adopt these values hereafter.

The curved solid lines in Fig. 9 show the magnetic-flux distributions around the fluxon center, calculated from Eqs. (40) and (44) using the parameters $\xi = 90$ nm, $\lambda = 50$ nm. It shows that the flux begins to spread even below the superconductor surface. The field distribution in the inner bulk region of the superconductor coincides with the original Clem model:

$$B_z(\rho) = \frac{\Phi_0}{2\pi\lambda\xi} \frac{K_0[(\rho^2 + \xi^2)^{1/2} / \lambda]}{K_1(\xi/\lambda)}, \quad (51)$$

where K_0 and K_1 are the modified Bessel functions. The result with a wider calculation area ($\rho = 0 - 2.5$ μm , $z = -0.5 - 2$ μm) is utilized for the comparisons with experimental results in Sec. VI.

The same calculation was performed for comparison using the literature values for the parameters of a polycrystalline thin film of lead,⁵⁵ $\xi = 76$ nm, $\lambda = 63$ nm. The calculated results are shown with curved dash-lines in Fig. 9. Although the difference between the curved solid

lines ($\xi = 90$ nm, $\lambda = 50$ nm) and the curved dash-lines are distinguished in the superconductor, it is vanishing in vacuum with the distance from the superconductor surface. As a matter of course, the flux distribution in vacuum reflects less the internal field distribution in the superconductor. Since our experiments could catch the flux distribution only above the superconductor surface, it is difficult to quantitatively determine the values of the GL parameters. The calculated results with the both pairs of parameters are utilized for the comparison with the experimental results.

For comparison, moreover, the magnetic-flux distribution is also calculated with an order parameter:

$$\Psi_1(\rho, \varphi, z) = \begin{cases} \left[1 - \exp\left[-\frac{\rho^2}{\xi^2}\right] \right] e^{-i\varphi} & (z \leq 0), \\ 0 & (z > 0), \end{cases} \quad (52)$$

instead of the Clem's one Eq. (44), using $\xi = 90$ nm, $\lambda = 50$ nm. The calculated results are shown with the curved dash lines in Fig. 10, indicating that the difference of the flux distribution between the Clem model and the model equation (52) is clear only near the fluxon center, and is vanishing in vacuum.

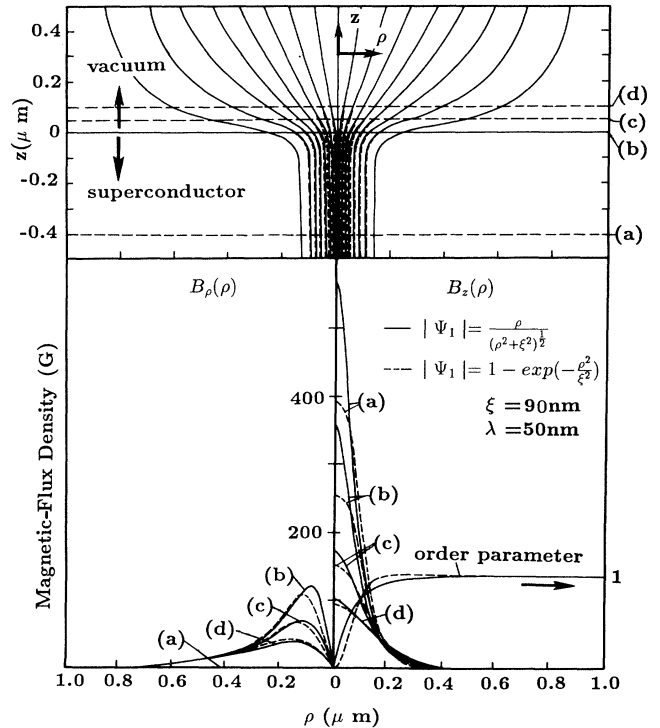


FIG. 10. The magnetic-flux distributions of a fluxon near the superconductor surface, calculated with the DEQSOL program using the GL equation Eq. (40). The curved solid lines are calculated with the Clem model Eq. (44), and the curved dash lines are with a model Eq. (52). Both are calculated with the parameters $\xi = 90$ nm, $\lambda = 50$ nm. The upper figure shows the flux-line distributions. The lower figure shows the profiles of the field distribution along the lines indicated in the upper figure. The field-vector components are separately shown.

According to Lasher,²⁰ the order parameter $\Psi_n(\rho)$ of a state consisting of MQF (n -flux quanta) is given in terms of that of the state of SQF $\Psi_1(\rho)$ as

$$\Psi_n(\rho) = \left[\Psi_1 \left(\frac{\rho}{\sqrt{n}} \right) \right]^n. \quad (53)$$

Then, using the Clem model Eq. (44), the order parameter of the MQF structure is given by

$$\Psi_n(\rho, \varphi, z) = \begin{cases} \left[\frac{\frac{\rho}{\sqrt{n}}}{\left[\frac{\rho^2}{n} + \xi^2 \right]^{1/2}} \right]^n e^{-in\varphi} & (z \leq 0), \\ 0 & (z > 0). \end{cases} \quad (54)$$

Figure 11 shows the calculated results from Eqs. (40) and (54) for $n=1$ and 4 using $\xi=90$ nm and $\lambda=50$ nm. The ordinate, flux density, in the lower figure is normalized for the flux density of a SQF. The difference of the flux distributions between the two models can be dis-

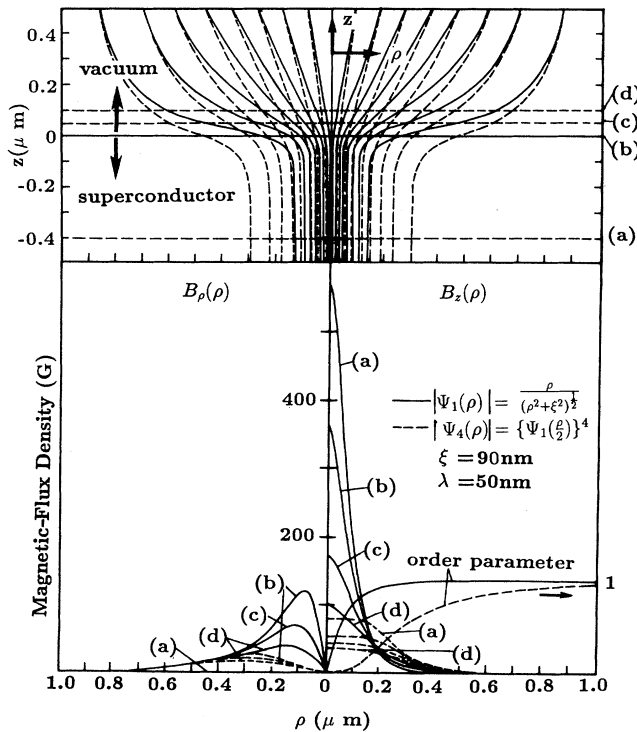


FIG. 11. The magnetic-flux distributions of a fluxon near the superconductor surface, calculated with the DEQSOL program using the GL equation Eq. (40). The curved solid lines are calculated with the Clem model Eq. (44), and the curved dash lines are with the Laser model Eq. (54). Both are calculated with the parameters $\xi=90$ nm, $\lambda=50$ nm. The upper figure shows the flux-line distributions. The lower figure shows the profiles of the field distribution along the lines indicated in the upper figure. The field-vector components are separately shown.

tinguished even in the vacuum above the superconductor surface.

For the SQF line in a film of thickness d , the flux distribution was calculated by utilizing Clem's order parameter;

$$\Psi_1(\rho, \varphi, z) = \begin{cases} 0 & (z > 0), \\ \frac{\rho}{(\rho^2 + \xi^2)^{1/2}} e^{-i\varphi} & (-d < z \leq 0), \\ 0 & (z \leq -d). \end{cases} \quad (55)$$

The calculated result using $\xi=90$ nm, $\lambda=50$ nm, from Eq. (40) with Eq. (55) for $d=4\lambda$ is shown in Fig. 12(b). It shows that the flux distribution just above the surface of the film is almost the same as that of the semi-infinite superconductor Fig. 12(a). We therefore utilize the results calculated for the semi-infinite superconductor for the comparison with the experimental results in Sec. VI.

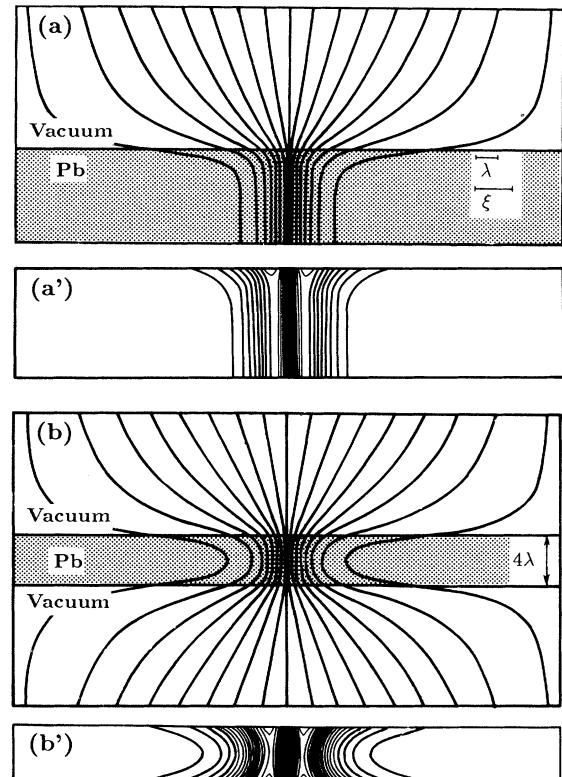


FIG. 12. The flux (upper figures) and circulating current (lower figures) distributions of a fluxon penetrating through (a) a semi-infinite and (b) a thin film of thickness $d=4\lambda$ of superconductors are calculated with the DEQSOL program using the GL equation Eq. (40) combined with the Clem models, Eqs. (44) and (55), respectively.

V. EXPERIMENTAL RESULTS

A. Observations of magnetic-flux structures

After the in-field cooling in which the film was cooled down from 15 to 4.2 K under the magnetic field of the fixed strengths, the holograms were taken during applying the field (in-field observation). We observed three kinds of magnetic-flux structures in superconducting lead films, depending on the film thickness and the applied magnetic field. Figure 13 shows the interference micrographs with π -phase interval, in which a single interference fringe exactly corresponds to a magnetic-flux line of a single flux quantum $h/2e$. The shadowed areas are the curved lead films and we can only observe the flux spreading out into vacuum after penetrating through the films. The observation areas for a lead film are not necessarily the same under the different applied magnetic fields.

Although the fluxons were observed in the 0.2- μm -thick film under the 1.0-Oe field, the fluxons did not appear under the fields below 2.0 Oe for the 1.0- μm -thick film, and below 5.0 Oe for the 1.7- μm -thick film. This fact indicates that the Meissner phase is extended into the higher field region with increase of the film thickness (see Fig. 1).

In the case of films of 0.2 μm thickness [Figs. 13(a)–13(c)], the fluxes penetrate in the form of the SQF lines, independent of the applied fields. They are the SQF structures of Tinkham.¹⁶ With an increase of the film thickness to 1.0 μm [Figs. 13(d)–13(f)], flux bundles with several flux quanta penetrate in the form of thin filaments, and their exits on the surface are pointlike. This is a MQF structure, which we call “MQF-*A* type” hereafter. In this structure, with the applied magnetic field, the amount of the flux contained in a single MQF line increases and the number of the MQF lines also increases. In the case of 1.7 μm [Figs. 13(g)–13(i)], moreover, the flux penetrate in the form of flux bundles, as in the case of the 1.0- μm -thick film. But the diameters of the flux bundles are much larger than those of the MQF-*A* lines. We call this structure “MQF-*B* type” from now on. In this case, with increase of the field strength, the diameters of the flux exits on the film surface seem to increase, although the diameters seems to remain unaltered in the MQF-*A* structure in the 1.0- μm -thick film. Figure 13 clearly shows three kinds of structures, SQF, MQF-*A*, and MQF-*B*, in the form of the distribution of magnetic flux lines. The differences between these structures will be more clearly shown in the detailed analysis of the internal field distributions around the fluxon center in the next subsection.

Although the SQF lines tend to arrange in the lattice form according to Tinkham,¹⁶ the observed SQF lines in the film of 0.2 μm seem to arrange at random. This is thought to be originated from the strong pinning force caused by the inhomogeneity of the film, the most prominent of which are grain boundaries.¹⁴ The arrangement can also be made random by the creation and annihilation of the vortex-antivortex pairs in the Kosterlitz-Thouless (KT) region¹⁵ just below the superconducting

transition temperature. KT theory has been extensively discussed concerning the melting of the flux line lattices in two-dimensional superconductors.^{56,57} The fluxon pairs observed in Figs. 13(a) and 13(b) may correspond to the ones predicted in KT theory. The pairs may have been created when the film was cooled down through the KT regime, and “frozen” by pinning so that the opposite fluxons would have not met to annihilate each other. The polarity of each fluxon is easily distinguished in the interference micrograph. Unless the polarities of the two fluxons are opposite, the fluxons individually stand up and fan out, not make a pair. This is one of the unique features to the electron holographic observation compared with other experimental methods. The pairs were not observed in the films of 1.0- μm and 1.7- μm thicknesses. This is naturally understood because KT theory is applicable only for the two-dimensional system, and on the contrary, for this reason, it is suggested that the observed flux pairs are the ones predicted by KT theory.

Figure 14(a) shows the interference micrograph of the SQF line appearing in the 0.2- μm -thick film under the 3.7-Oe field, in which a single fringe exactly corresponds to a single flux quantum. Figure 14(b) is a phase-difference-amplified interference micrograph⁴² analyzed from the same hologram as Fig. 14(a). This micrograph was obtained by setting the contour phase lines at $\pi/4$ phase intervals, instead of π interval in Fig. 14(a), from the phase data numerically measured by the fringe scanning interferometry. This is called “eight-times amplified” so that a single fringe corresponds to a magnetic flux line of $h/8e$. The total amount of flux and the detailed flux distribution can be estimated with higher accuracy.

The MQF-*A* lines with four flux quanta emerging in the 1.0- μm -thick film under the 5.0-Oe field are shown in Figs. 15(a), and 15(b) is its eight-times phase-difference-amplified interference micrograph in which a single fringe corresponds to a magnetic flux line of $h/8e$. The flux penetrating through the superconductor looks as fine as that of the SQF in Fig. 14.

Figure 16 shows the MQF-*B* lines with four flux quanta appearing on the 1.7- μm -thick film under the field of 12.2 Oe. The root of the flux is much broader than that of the MQF-*A* line in Fig. 15, while the amounts of the flux are the same.

In this way, the structural changes from the SQF to the MQF-*A* and the MQF-*B* structures are clearly and directly shown in the form of magnetic-flux distributions in interference micrographs. The changes seem to originate only from the increase of the film thickness, because, from the R_R measurement, the quality of the films is estimated to remain unaltered with the thickness change.

B. Internal field distributions of quantized magnetic fluxes

The phase distributions of the electron waves transmitted through the fluxons were numerically measured and then the field vector components around the fluxon centers were decomposed using the digital phase analysis

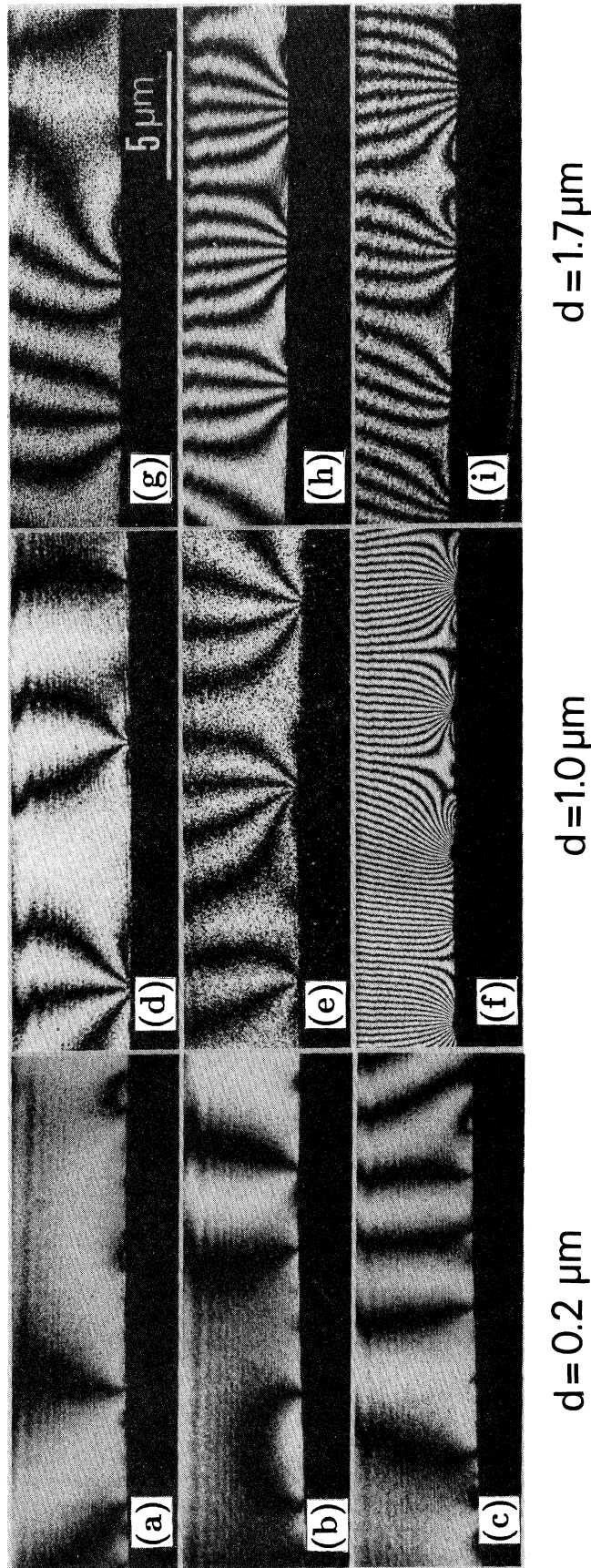


FIG. 13. Interference micrographs with phase interval of π showing the quantized magnetic fluxes appearing on the surfaces of the superconducting lead films. A single interference fringe exactly corresponds to a single flux quantum, $h/2e$. The magnetic-flux structures vary depending on the film thickness d and the applied field H . (a) $H = 1.6$ Oe, (b) $H = 3.7$ Oe, (c) $H = 5.0$ Oe for $d = 0.2$ μm . (d) $H = 3.7$ Oe, (e) $H = 5.0$ Oe, (f) $H = 18.3$ Oe for $d = 1.0$ μm . (g) $H = 7.5$ Oe, (h) $H = 12.2$ Oe, (i) $H = 18.3$ Oe for $d = 1.7$ μm .

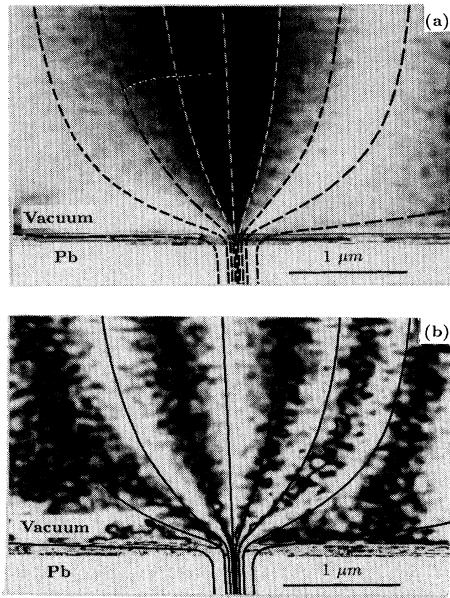


FIG. 14. A singly quantized flux (SQF) line appearing in the 0.2- μm -thick lead film under the 3.7-Oe field. (a) Interference micrograph showing the flux lines in units of $h/2e$, and (b) in units of $h/8e$ (an eight-times phase-difference amplified interference micrograph). The curved dash lines in (a) and the curved solid lines in (b) are the flux distribution calculated from the GL equation Eq. (40) with the Clem model equation (44) using the parameters $\xi=90$ nm, $\lambda=50$ nm.

method as described in Sec. III.

At first, we analyzed the hologram taken from the 1.0- μm -thick lead film under the 5.0-Oe field (MQF-*A*). Figure 17(b) shows the line profile of the phase distribution along the line *AA* just above the superconductor surface in the interference micrograph Fig. 17(a). It shows that the phase steeply shifts at the flux exits and does not shift between them. This shows the Aharonov-Bohm effect.

The wave front numerically reconstructed in this way is three dimensionally displayed in Fig. 18. The near side of the wave front ($z=0$) is adjacent to the lead film surface. This wave front is an expected one shown in Fig. 4. The sudden phase shifts at the flux exits are multiples of π , and their multiples are the number of fringes in Fig. 17(a). This fact precisely means the flux quantization in units of $h/2e$. The phase measurement precision in the fringe scanning interferometry⁷ corresponds to the flux resolution of $\sim h/100e$.

On the next step, the field-vector components were derived from the numerically measured phase distributions by the data processing method mentioned in Sec. III. The derivative $\partial\phi(x,z)/\partial x$ is calculated from the phase profile Fig. 17(b) and presented in Fig. 17(c). It has peaks at the flux exits because it is the line integral of the field-vector component B_z normal to the surface along the electron path as expressed by Eq. (23). In the same way Fig. 17(d) is the derivative $\partial\phi(x,z)/\partial z$ which corresponds to Eq. (24). Using these data, then, the field-vector com-

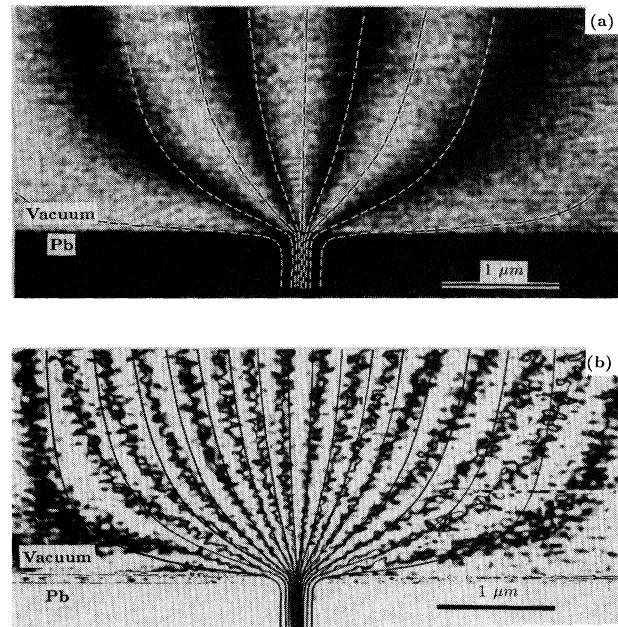


FIG. 15. A multiply quantized flux (MQF-*A*) line appearing on the 1.0- μm -thick lead film under the 5.0-Oe field. (a) Interference micrograph showing the flux lines in units of $h/2e$ and (b) in units of $h/8e$ (an eight-times phase-difference amplified interference micrograph). The curved dash-lines in (a) and the curved solid lines in (b) are the flux distribution calculated from the GL equation Eq. (40) with the Clem model equation (44) using the parameters $\xi=90$ nm, $\lambda=50$ nm.

ponents were calculated according to Eqs. (25), (32), (33), and (34). The solid broken lines in Fig. 19 show the result obtained from the flux bundle with four-flux quanta appearing at the left end of Fig. 17(a) or Fig. 15. The ordinate is normalized for the flux density of a SQF. Electron holography combined with the digital phase analysis method in this way enables the quantitative measurement of the field-vector components near the center of an *individual* flux in terms of the distance from the core axis.

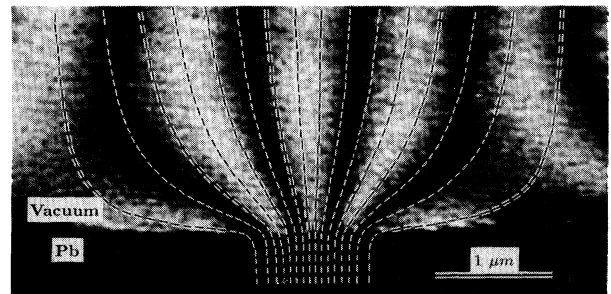


FIG. 16. A multiply quantized flux (MQF-*B*) line appearing on the 1.7- μm -thick lead film under the 12.2-Oe field. An interference fringe corresponds to the flux quantum $h/2e$. The curved dash lines shows the flux distribution calculated from the GL equation Eq. (40) with a model Eq. (59) with $R=0.4$ μm , $\xi=90$ nm, $\lambda=50$ nm.

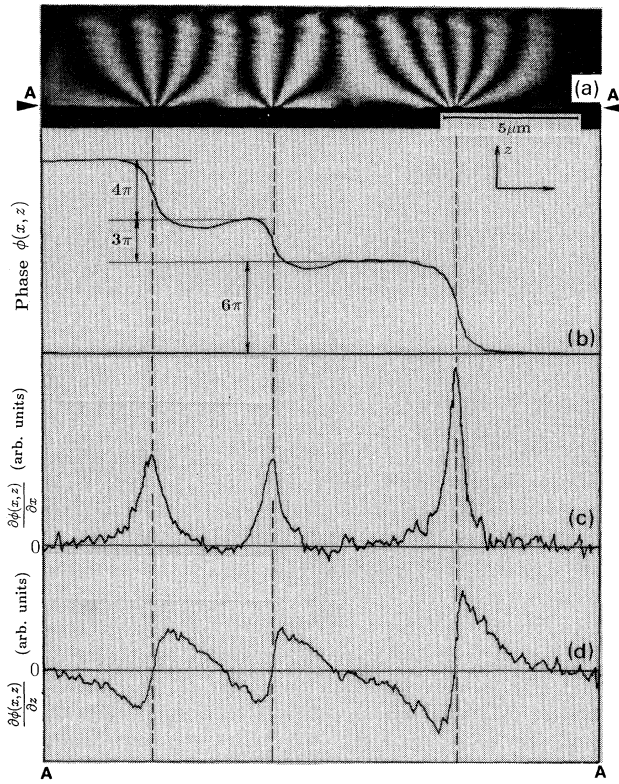


FIG. 17. Digital phase analysis for the fluxes appearing on the 1.0- μm -thick film under the 5.0-Oe field. (a) Interference micrograph showing the MQF-*A* structure. (b) Line profile of the phase distribution along the line *AA* just above the superconductor surface in the micrograph (a). (c) Its derivative with x , $\partial\phi(x, z)/\partial x$. (d) Its derivative with z , $\partial\phi(x, z)/\partial z$.

The same analysis for the SQF line shown in Fig. 14 was carried out, and its result is shown as the broken dash lines in Fig. 19. The field distributions of the SQF and MQF-*A* almost coincide.

We next analyzed the flux of the MQF-*B* structure in the 1.7- μm -thick film under the 12.2-Oe field. Figure 20(b) is the line profile of the phase distribution along the

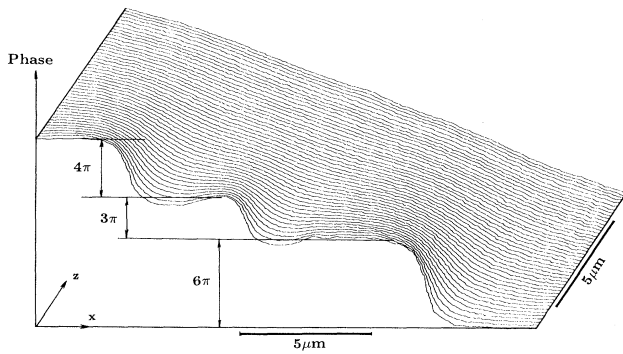


FIG. 18. Electron wave front reconstructed by the digital phase analysis method. The hologram taken from the MQF-*A* structure shown in Fig. 17 was analyzed. The near side of the wave front ($z=0$) is adjacent to the lead film surface.

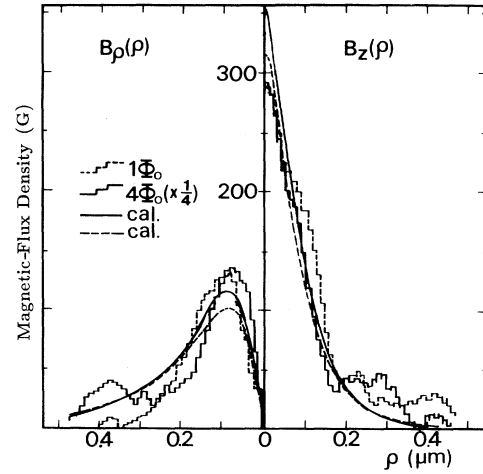


FIG. 19. Field-vector components, $B_z(\rho)$, normal to the surface, and $B_\rho(\rho)$, parallel to the surface, around the flux center just above the superconducting lead film surfaces. The broken dash lines are for the SQF line shown in Fig. 14. The broken solid lines are for the MQF-*A* line shown in Fig. 15. The curved solid lines are the distributions calculated from the GL equation Eq. (40) with the Clem model equation (44) using the parameters $\xi=90$ nm, $\lambda=50$ nm. The curved dash lines are the calculated ones with the parameters $\xi=76$ nm, $\lambda=63$ nm.

line *AA* just above the superconductor surface in the interference micrograph (a). Since, as in Fig. 17, the phase shifts at the flux exist are multiples of π , it is included that the fluxes are quantized in units of $h/2e$. But the phase changes are slower in broader areas compared with those in Fig. 17, which means the lower flux density in the MQF-*B* compared with that of the SQF and MQF-*A* lines. The derivatives $\partial\phi(x, z)/\partial x$ and $\partial\phi(x, z)/\partial z$ were calculated and shown in Figs. 20(c) and 20(d). We analyzed the field components of the flux with four-flux quanta appearing at the left end in this figure. The result shown in Fig. 21 is apparently different from the ones in Fig. 19. The B_z distribution shows, in particular, the nearly uniform flux penetration through a semimacroscopic normal region.

By introducing the digital phase analysis method, in this way, we cannot only determine the flux amounts with much higher accuracy compared with the interference micrograph observation, but also analyze the internal-field distributions in three dimensions.

VI. DISCUSSIONS

A. Detection of a single fluxon

The contrast produced by a single fluxon in Lorentz microscopy have been calculated by several authors^{3,58-61} to find that the position detection of a single fluxon is near the observation limit from the uncertainty principle.

Using the phase difference $d\phi$ between the two paths 1

and 2 in Fig. 8, $d\phi = (\partial\phi/\partial x)dx$, the deflection angle of the incident electron beam β by the magnetic field of a single fluxon is given by $\beta = d\phi/k_y dx$, where k_y is the y component of the wave number vector of the incident electron. The phase difference $d\phi$ is expressed with the amount of the flux between the two paths $d\Phi$ as $d\phi = \pi d\Phi/\Phi_0$ [Eq. (16)], where $\Phi_0 = h/2e$. The momentum change of the incident electron beam in the x direction dp_x , on the other hand, is given by $dp_x = p_y \beta$, where p_y is the momentum component in the incident direction. Consequently we get

$$dp_x dx = \frac{h}{2} \frac{d\Phi}{\Phi_0}. \quad (56)$$

On the other hand, the spread Δx of the wave packet in the x direction consisting of plane waves with the momentum uncertainty dp_x is related by

$$dp_x \Delta x \geq h, \quad (57)$$

from the uncertainty principle. Since the spatial resolution of real observations dx is always $dx \geq \Delta x$, we get

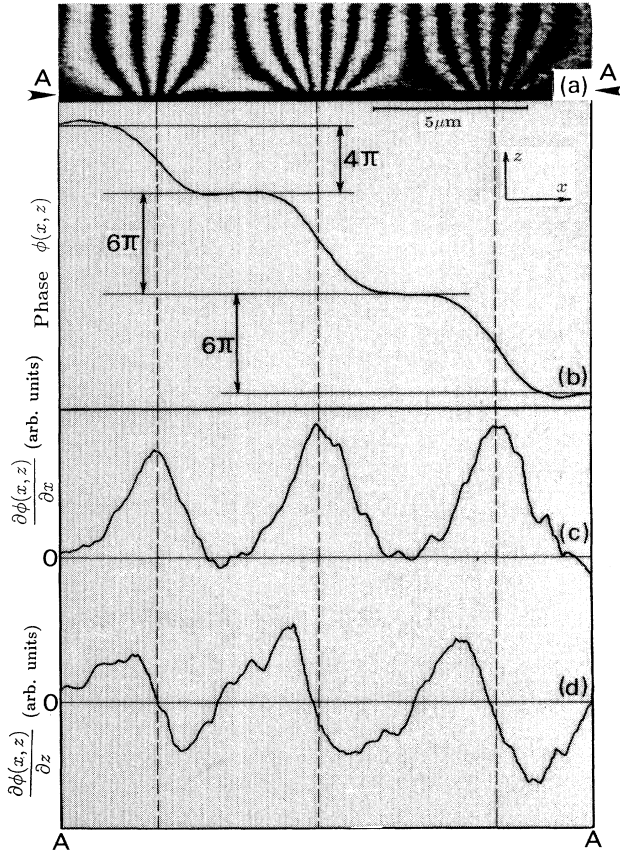


FIG. 20. Digital phase analysis for the fluxes appearing on the 1.7- μm -thick film under the 12.2-Oe field. (a) Interference micrograph showing the MQF-B structure. (b) Line profile of the phase distribution along the line AA just above the superconductor surface in the micrograph (a). (c) Its derivative with x , $\partial\phi(x, z)/\partial x$. (d) Its derivative with z , $\partial\phi(x, z)/\partial z$.

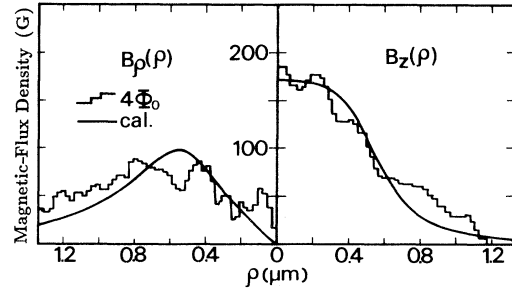


FIG. 21. Field-vector components, $B_z(\rho)$, normal to the surface, and $B_\rho(\rho)$, parallel to the surface, around the flux center just above the superconducting lead film surfaces. The broken solid lines are the flux distribution in the MQF-B line shown in Fig. 16. The curved solid lines are the distribution calculated from the GL equation Eq. (40) with a model Eq. (59) with $R = 0.4 \mu\text{m}$, $\xi = 90 \text{ nm}$, $\lambda = 50 \text{ nm}$.

therefore, from Eqs. (56) and (57),

$$\frac{d\Phi}{\Phi_0} \geq 2. \quad (58)$$

This implies that the observation of magnetic fluxes with spatial resolution of dx needs the flux (change) of order of Φ_0 in the interval of dx . In other words, in the case of the observation of a single fluxon, its position can be determined only with the precision of order of its diameter.

The present report, however, shows the observation of a single fluxon with the flux resolution $d\Phi \sim \Phi_0/100$ and the spatial resolution dx of approximately one-hundredth of its diameter. This seems to contradict the uncertainty principle mentioned above.

A classical picture such as the above discussion on the connection between the spatial and flux resolutions is not applicable to the electron holography. The observation in image-electron holography is carried out essentially in quantum mechanics. The spatial resolution is not determined by the wave packet spread in the direction perpendicular to the propagation. In our holography electron microscope, the electron wave packet widely spread $\sim 50 \mu\text{m}$ in the x direction at the specimen plane. Utilizing a part of the wave packet as an object wave, an in-focused image is formed with spatial resolution as high as conventional electron microscopes. The remaining part of the wave packet is utilized as a reference wave. The high resolution for magnetic fluxes is achieved by interfering the object wave with the reference one, irrespective of the spatial resolution of the image. Utilizing the reference wave in the electron holography, the high resolution for magnetic fluxes can be obtained without any reduction of the spatial resolution.

B. Magnetic flux structures of lead films

Now we compare the experimental and calculated results on the internal field distributions of quantized fluxes. The curved dash lines in Fig. 14(a) show the flux distribution calculated from the GL equation Eq. (40)

with the Clem model Eq. (44) for the SQF line using the parameters $\xi=90$ nm, $\lambda=50$ nm. The observed and calculated distributions qualitatively agree, implying that we actually observed the flux exit just on the superconductor surface. More detailed comparison is possible in Fig. 14(b) with a phase-difference-amplified interference micrograph.⁴² The calculated distribution (curved solid lines) considerably agrees, particularly at the flux root just above the surface.

In the case of the MQF-*A* line in Fig. 15, the agreement with the calculated distribution with the Clem model, which is the same as that of the SQF line in Fig. 14, is also considerable. Since, as shown in Fig. 11, the difference of the magnetic-flux distribution between the Clem model Eq. (44) and the Lasher model Eq. (54) for the MQF lines ($n=4$) is evident, we can conclude from our observation that the MQF-*A* structure is better described by Clem's order parameter for the SQF line than that of Lasher's for n -quanta MQF line. Figures 14 and 15 show that the field distributions around the center of the SQF and MQF-*A* lines are in the same character with the exception of their flux amounts.

At the region far from the surface in the images of Figs. 14 and 15, the calculated lines slightly deviate from the observed ones because of the boundary conditions for solving the GL equations. Equation (45) does not accurately reflect the real circumstances, which affect the distributions at the circumference in the images. Experimentally, moreover, the fringe distributions at the region far from the superconductor surface are apparently affected by the slight inclination of the mirrors in the optical reconstruction interferometer (Fig. 6). Anyway, our main interest lies in the internal field distribution at the flux root just on the surface.

As mentioned in the previous section, the root of the MQF-*B* line shown in Fig. 16 seems much broader than those of the SQF and the MQF-*A* lines. This feature is qualitatively explained by the Lasher's order parameter Eq. (54) for the MQF line as shown in Fig. 11, which, however, does not give quantitative agreement satisfactorily with the observed MQF-*B* line. In order to better simulate the flux distribution of the MQF-*B* line shown in Fig. 16, we assume an order parameter

$$\Psi(\rho, \varphi, z) = \begin{cases} \{1 - e^{-(\rho-R)^2/\xi^2}\}^{1/2} e^{-in\varphi} & (z < 0, \rho > R), \\ 0 & (z < 0, 0 \leq \rho \leq R), \\ 0 & (z \geq 0), \end{cases} \quad (59)$$

instead of Eq. (54). This model implies that a circular normal region of the radius R appears in the superconducting phase and the magnetic-flux bundle of n quanta penetrates therein. The curved dash lines in Fig. 16 show the flux distribution calculated from the GL equation Eq. (40) using this model of $R=0.4$ μm , $n=4$, $\xi=90$ nm, and $\lambda=50$ nm. The agreement of the observed pattern is fairly good, which shows distinct difference from the SQF and the MQF-*A* lines.

The field-vector components are also compared. The

curved solid lines and the curved dash lines in Fig. 19 show the calculated distributions with Clem's order parameter Eq. (44) using the parameters $\xi=90$ nm, $\lambda=50$ nm, and $\xi=76$ nm, $\lambda=63$ nm, respectively (compare with the curved lines in Fig. 9). The experimental results for the SQF (broken dash lines) and the MQF-*A* (broken solid lines) are considerably traced by the calculated curves. The MQF-*A* line, in particular, penetrates in the form of a filament as fine as the SQF line. We cannot obtain here a definite conclusion which pair of the GL parameters here adopted in the calculation is more appropriate.

Concerning the MQF-*B* line, the curved solid lines in Fig. 21 are calculated with a model Eq. (59), which fairly well traces the experimental results (broken solid lines). This field distribution cannot be explained by any curves in Fig. 9, implying that the broadening of the flux root in the MQF-*B* line is intrinsic, not due to the shadowing of a finer root by the curved lead film edge.

It should be pointed out here that the flux density just above the normal region on the superconductor surface in the MQF-*B* structure is estimated approximately 180 G from Fig. 21, which is much lower than the thermodynamical critical field ~ 500 G of bulk superconducting lead at $T=4.2$ K. The internal field in the normal domain in a macroscopic intermediate state, on the other hand, is expected to be approximated by the thermodynamic critical field. This extraordinary reduction of the flux density in the normal region of the MQF-*B* structure is considered to come from the surface and size effects. As estimated in Sec. IV and observed in Sec. V, the flux lines rapidly disperse out from the superconductor surface, and its flux density fairly decreases even near the center of the normal region compared with that in the inner bulk region. Since the MQF-*B* lines, moreover, have much smaller size in geometry compared with a macroscopic intermediate state, its characteristics such as the flux density in the normal region can be different from that of the intermediate state in a bulk superconductor. For instance, certain reduction of the critical field in thin films has been observed.^{31,32}

Another remark remains to be made concerning the implication of the observed MQF-*A* and MQF-*B* lines. They do not directly correspond to the Lasher's MQF and the Goren's NS structures, respectively. They predicted their structures only applicable at relatively high field regions, while our observations were carried out under very weak fields, just above the "lower critical field" $(1-D)H_c$ (see Fig. 1). Since the critical value of the GL parameter κ for the transition between type-I and -II behaviors in superconducting characteristics is predicted to be $\kappa=1/\sqrt{2}=0.707$ from the original GL theory, the estimated values $\kappa=0.56-0.59$ for our lead films at $T=4.2$ K seem to be considerably small for the transition. Detailed investigations, however, have revealed the attractive interaction among fluxons in a narrow κ range near $\kappa=1/\sqrt{2}$, called the intermediate-mixed state.^{24,25,32} Auer and Ullmaier⁶² observed the transition from type-I to -II states at κ values as small as 0.6 in the range of low temperature $T/T_c < 0.4$. The phase diagram in which type-I and type-II states including the intermediate-

mixed state are classified in terms of κ and T , has been investigated by many researchers.¹ Our observed MQF-*A* and MQF-*B* structures, therefore, may be understood as some transition characteristics between type-I and -II superconductors. Besides this effect, some additional features such as the pinning⁹ and surface effects may raise the variety of magnetic-flux structures like the MQF-*A* and MQF-*B* lines under low magnetic fields.

VII. SUMMARY

1. We have succeeded to directly image a singly quantized flux emerging on the surface of superconducting lead films in the form of magnetic-flux line distributions using the electron holography technique. Combining the digital phase analysis method, furthermore, the flux quantum $h/2e$ have been determined for individual fluxes with prediction of $\sim h/100e$. This method has also allowed one to analyze in detail the distributions of the field-vector components around individual fluxon centers.

2. The fluxon pairs, consisting of two antiparallel fluxons, have been observed only in the lead films of 0.2 μm thickness, not in thicker films. These may be the ones predicted by Kosterlitz-Thouless theory.

3. Under certain restricted observation conditions, i.e., under low fields and low temperatures, we have clearly observed the changes of the magnetic-flux structures of superconducting lead films with increase of the film thickness. In addition to the singly quantized flux structure in the 0.2- μm -thick films, two types of the multiply quantized flux structures have been newly observed in thicker films.

4. We have numerically solved the Ginzburg-Landau equations to calculate the field distributions around the fluxon center near the superconductor surface. Considerable agreement between the calculated and the experimental results was obtained. In particular, the internal field distribution of the MQF-*A* line appearing in the 1.0- μm -thick lead film has been found to be the same as that of the SQF line in the 0.2- μm -thick film.

ACKNOWLEDGMENTS

We would like to express our appreciation for the guidance and encouragement on fringe scanning interferometry received from Professor Toyohiko Yatagai of

Tsukuba University. We also gratefully acknowledge helpful discussions with Dr. Ushio Kawabe, Dr. Yoshinobu Tarutani of Hitachi Central Research Laboratory (CRL). Dr. Seiji Saito and Dr. Toshiyuki Onogi of Hitachi Advance Research Laboratory (ARL) drew our attention to the theoretical aspects on the fluxon core structure. Dr. Masaaki Futamoto and Dr. Yukio Honda of CRL made encouraging suggestions on the sample preparation. Miyuki Saji of CRL assisted the numerical calculation with the DEQSOL program. Our colleagues at ARL, Takeshi Tawasaki, Takao Matsumoto, Hiroto Kasai, Dr. Hiroshi Kajiyama, Hisashi Nagano, and Seichi Kondo helped with the experiments.

APPENDIX: CALCULATING THE B_ρ COMPONENT FROM THE PHASE DISTRIBUTION

We derive Eq. (33) from Eq. (24) by the similar method with the case of the B_z -component derivation. Transforming into the cylindrical coordinate, Eq. (24) is rewritten as

$$\frac{\partial\phi(x,z)}{\partial z} = \frac{e}{\hbar} \int_{-\infty}^{\infty} dy B_\rho(\rho,z) \cos\varphi. \quad (\text{A1})$$

Taking the Fourier transform with respect to x ,

$$\begin{aligned} S(X,z) &= \int_{-\infty}^{\infty} dx \frac{\partial\phi(x,z)}{\partial z} e^{2\pi i x X} \\ &= \frac{e}{\hbar} \int_{-\infty}^{\infty} dx \int_{-\infty}^{\infty} dy B_\rho(\rho,z) \cos\varphi e^{2\pi i x X} \\ &= \frac{e}{\hbar} \int_0^{2\pi} d\varphi \int_0^{\infty} d\rho \rho B_\rho(\rho,z) \cos\varphi e^{2\pi i \rho X \cos\varphi}. \quad (\text{A2}) \end{aligned}$$

The φ integral can be performed by taking into account the definition of the Bessel function Eq. (27):

$$S(X,z) = \frac{2\pi i e}{\hbar} \int_0^{\infty} d\rho \rho B_\rho(\rho,z) J_1(2\pi\rho X). \quad (\text{A3})$$

After multiplying $XJ_1(2\pi tX)$ to both sides of Eq. (A3), and integrating with X , we get

$$\int_0^{\infty} dX X S(X,z) J_1(2\pi tX) = \frac{2\pi i e}{\hbar} \int_0^{\infty} d\rho \int_0^{\infty} dX \rho X B_\rho(\rho,z) J_1(2\pi\rho X) J_1(2\pi tX). \quad (\text{A4})$$

By replacing $\eta = 2\pi X$, the right-hand side of Eq. (A4) is

$$\frac{ie}{2\pi\hbar} \int_0^{\infty} d\rho \int_0^{\infty} d\eta \rho \eta B_\rho(\rho,z) J_1(\rho\eta) J_1(t\eta). \quad (\text{A5})$$

Using the identity Eq. (31), Eq. (A5) is equivalent to

$(ie/2\pi\hbar)B_\rho(t,z)$. Consequently Eq. (A4) is reduced to Eq. (33):

$$B_\rho(\rho,z) = \frac{2\pi\hbar}{ie} \int_0^{\infty} dX X S(X,z) J_1(2\pi\rho X). \quad (\text{A6})$$

*Present address: Department of Physics, Faculty of Science, University of Tokyo, Hongo, Bunkyo-ku, Tokyo 113, Japan.

¹R. P. Huebener, *Magnetic Flux Structures in Superconductors* (Springer-Verlag, New York, 1979).

²For example, M. Tinkham, *Introduction to Superconductivity* (McGraw-Hill, New York, 1975).

³T. Suzuki and A. Seeger, *Comments Solid State Phys.* **3**, 128, 173 (1971).

- ⁴H. Boersch, B. Lischke, and H. Solling, *Phys. Status Solidi* **61**, 215 (1974).
- ⁵T. Matsuda, S. Hasegawa, M. Igarashi, T. Kobayashi, M. Naito, H. Kajiyama, J. Endo, N. Osakabe, A. Tonomura, and R. Aoki, *Phys. Rev. Lett.* **62**, 2519 (1989).
- ⁶T. Yatagai, K. Ohmura, S. Iwasaki, S. Hasegawa, J. Endo, and A. Tonomura, *Appl. Opt.* **26**, 377 (1987).
- ⁷S. Hasegawa, T. Kawasaki, J. Endo, A. Tonomura, Y. Honda, M. Futamoto, K. Yoshida, F. Kugiyu, and M. Koizumi, *J. Appl. Phys.* **65**, 2000 (1989).
- ⁸J. R. Clem, *J. Low Temp. Phys.* **18**, 427 (1975).
- ⁹T. Barbee, *Appl. Phys. Lett.* **14**, 156 (1969).
- ¹⁰H. Hoersch, U. Kunze, B. Lischke, and W. Rodewald, *Phys. Lett.* **44A**, 273 (1973).
- ¹¹B. Lischke and W. Rodewald, *Phys. Status Solidi B* **63**, 97 (1974); **62**, 377 (1974).
- ¹²W. Rodewald, *Phys. Lett.* **55A**, 135 (1975); thesis, Technischen Universität Berlin (1977).
- ¹³G. J. Dolan and J. Silcox, *Phys. Rev. Lett.* **30**, 603 (1973).
- ¹⁴G. J. Dolan, *J. Low Temp. Phys.* **15**, 111 (1974); **15**, 133 (1974).
- ¹⁵J. M. Kosterlitz and D. Thouless, *J. Phys. C* **6**, 1181 (1973).
- ¹⁶M. Tinkham, *Phys. Rev.* **129**, 2413 (1963); *Rev. Mod. Phys.* **36**, 268 (1964).
- ¹⁷E. Guyon, C. Caroli, A. Martinet, *J. Phys. Radium* **25**, 683 (1964).
- ¹⁸J. Pearl, *Appl. Lett.* **5**, 65 (1964); *J. Appl. Phys.* **37**, 4139 (1966).
- ¹⁹K. Maki, *Ann. Phys. (N.Y.)* **34**, 363 (1965).
- ²⁰G. Lasher, *Phys. Rev.* **154**, 345 (1967); **140**, A523 (1965).
- ²¹A. L. Fetter and P. C. Hohenberg, *Phys. Rev.* **159**, 330 (1967).
- ²²R. N. Goren and M. Tinkham, *J. Low Temp. Phys.* **5**, 465 (1971).
- ²³U. Essman and H. Träuble, *Phys. Lett.* **24A**, 526 (1967).
- ²⁴H. Träuble and U. Essman, *J. Appl. Phys.* **39**, 4052 (1968); *J. Sci. Instrum.* **43**, 344 (1966); *Phys. Status Solidi* **18**, 813 (1966); **20**, 95 (1967); **25**, 373 (1968); **25**, 395 (1968).
- ²⁵N. V. Sarma, *Phys. Lett.* **25A**, 315 (1967); *Philos. Mag.* **17**, 1233 (1968); **18**, 171 (1968).
- ²⁶A. L. Schawlow, *Phys. Rev.* **101**, 573 (1956).
- ²⁷U. Krögeloh, *Phys. Lett.* **28A**, 657 (1969).
- ²⁸B. Obst, *Phys. Status Solidi B* **45**, 453 (1971); **45**, 467 (1971).
- ²⁹A. Bodmer, U. Essman, and H. Träuble, *Phys. Status Solidi A* **13**, 471 (1972).
- ³⁰C. P. Herring, *Phys. Lett.* **47A**, 105 (1974).
- ³¹G. D. Cody and R. E. Miller, *Phys. Rev.* **173**, 481 (1968); **5**, B1834 (1972).
- ³²R. E. Miller and G. D. Cody, *Phys. Rev.* **173**, 494 (1968); **173**, B1834 (1972).
- ³³B. L. Brandt, R. D. Parks, and R. D. Chaudhari, *J. Low Temp. Phys.* **4**, 41 (1971).
- ³⁴M. D. Maloney, F. de la Cruz, and M. Cordona, *Phys. Rev. B* **5**, 3558 (1972).
- ³⁵E. H. Brandt, *J. Low Temp. Phys.* **73**, 355 (1988).
- ³⁶D. Cribier, B. Jacrot, L. M. Rao, and B. Farnoux, *Phys. Lett.* **9**, 106 (1964).
- ³⁷G. Pozzi and U. Valdre, *Philos. Mag.* **23**, 745 (1971).
- ³⁸E. H. Darlington and U. Valdre, *J. Phys. E* **8**, 321 (1975).
- ³⁹H. F. Hess, R. B. Robinson, R. C. Dynes, J. M. Valles, Jr., and J. V. Waszczak, *Phys. Rev. Lett.* **62**, 214 (1989); **64**, 2711 (1990).
- ⁴⁰B. Shinozaki, R. Aoki, T. Miyazaki, M. Katayama, and S. Yamashita, *J. Phys. Soc. Jpn.* **50**, 1868 (1981).
- ⁴¹D. Gabor, *Proc. R. Soc. London* **A197**, 454 (1949); **B64**, 449 (1951).
- ⁴²A. Tonomura, *Rev. Mod. Phys.* **59**, 639 (1987).
- ⁴³Y. Aharonov and D. Bohm, *Phys. Rev.* **115**, 485 (1959).
- ⁴⁴A. Tonomura, N. Osakabe, T. Matsuda, T. Kawasaki, J. Endo, S. Yano, and H. Yamada, *Phys. Rev. Lett.* **56**, 792 (1986).
- ⁴⁵R. Koepke and G. Bergmann, *Z. Phys.* **242**, 31 (1971).
- ⁴⁶G. Brandli and J. L. Olsen, *Mater. Sci. Eng.* **4**, 61 (1969).
- ⁴⁷K. Fuchs, *Proc. Cambridge Philos. Soc.* **34**, 100 (1938); E. H. Sondheimer, *Adv. Phys.* **1**, 1 (1952).
- ⁴⁸G. Möllenstedt and H. Dücker, *Naturwissenschaften* **42**, 41 (1955).
- ⁴⁹J. H. Bruning, D. R. Herriot, D. P. Rosenfeld, A. D. White, and D. J. Brangaccio, *Appl. Opt.* **13**, 2693 (1974).
- ⁵⁰D. J. DeRosier and A. Klug, *Nature (London)* **217**, 130 (1968).
- ⁵¹F. London, *Superfluids* (Wiley, New York, 1950), Vol. 1, p. 143.
- ⁵²G. Eilenberger, *Z. Phys.* **214**, 195 (1968).
- ⁵³C. Kon'no, M. Saji, N. Sagawa, and Y. Umetani, in *Proceedings of the Fall Joint Computer Conference*, 1026, Dallas (IEEE Computer Society Press, Washington, DC, 1986).
- ⁵⁴M. Tinkham, in *Low Temperature Physics*, edited by C. DeWitt, B. Dreyfus, and P. G. de Gennes (Gordon and Breach, New York, 1962), p. 166.
- ⁵⁵G. E. Peabody and R. Meserve, *Phys. Rev. B* **6**, 2579 (1972).
- ⁵⁶B. A. Huberman and S. Doniach, *Phys. Rev. Lett.* **43**, 959 (1979).
- ⁵⁷D. S. Fisher, *Phys. Rev. B* **22**, 1190 (1980).
- ⁵⁸D. Wohlleben, *J. Appl. Phys.* **38**, 3341 (1967).
- ⁵⁹H. Yoshioka, *J. Phys. Soc. Jpn.* **21**, 948 (1966).
- ⁶⁰M. J. Goring and J. P. Jakubovics, *Philos. Mag.* **15**, 393 (1967).
- ⁶¹C. Capiluppi, G. Pozzi, and U. Valdre, *Philos. Mag.* **26**, 865 (1972).
- ⁶²J. Auer and H. Ullmaier, *Phys. Rev. B* **7**, 136 (1973).

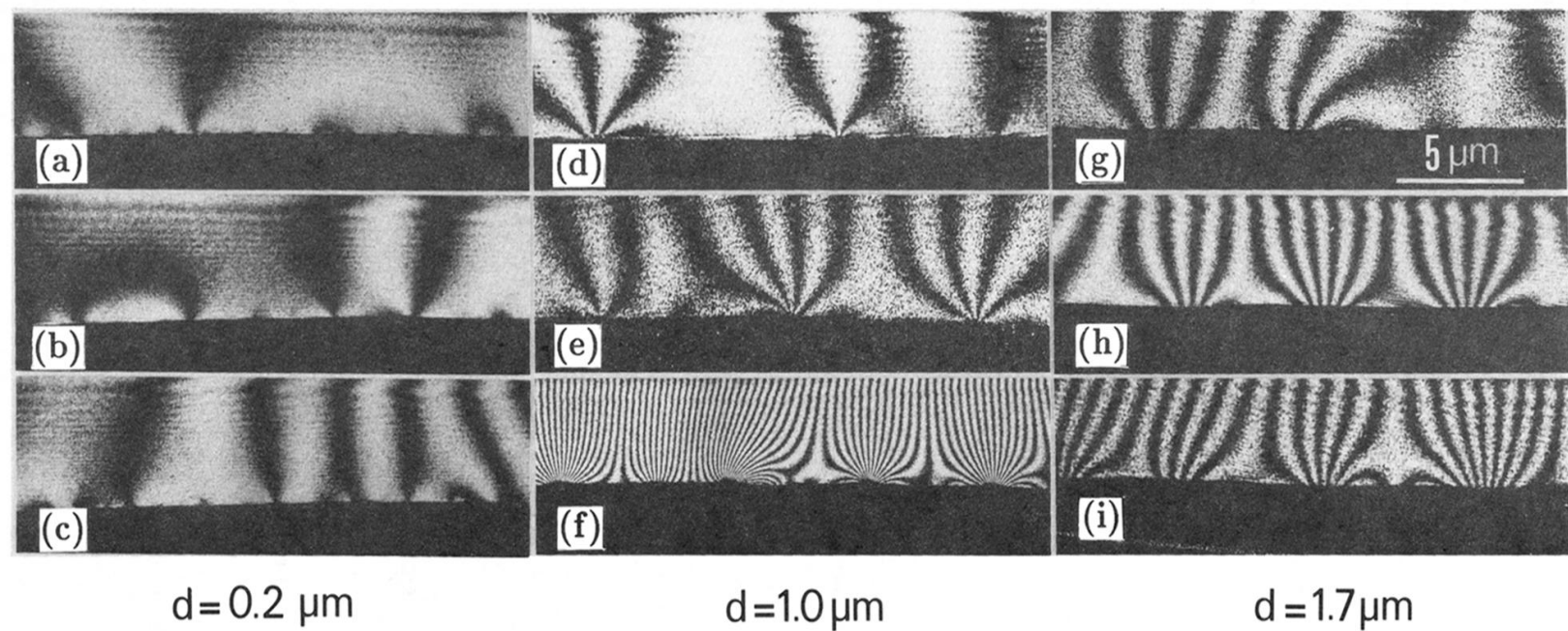


FIG. 13. Interference micrographs with phase interval of π showing the quantized magnetic fluxes appearing on the surfaces of the superconducting lead films. A single interference fringe exactly corresponds to a single flux quantum, $h/2e$. The magnetic-flux structures vary depending on the film thickness d and the applied field H . (a) $H = 1.6$ Oe, (b) $H = 3.7$ Oe, (c) $H = 5.0$ Oe for $d = 0.2 \mu\text{m}$. (d) $H = 3.7$ Oe, (e) $H = 5.0$ Oe, (f) $H = 18.3$ Oe for $d = 1.0 \mu\text{m}$. (g) $H = 7.5$ Oe, (h) $H = 12.2$ Oe, (i) $H = 18.3$ Oe for $d = 1.7 \mu\text{m}$.

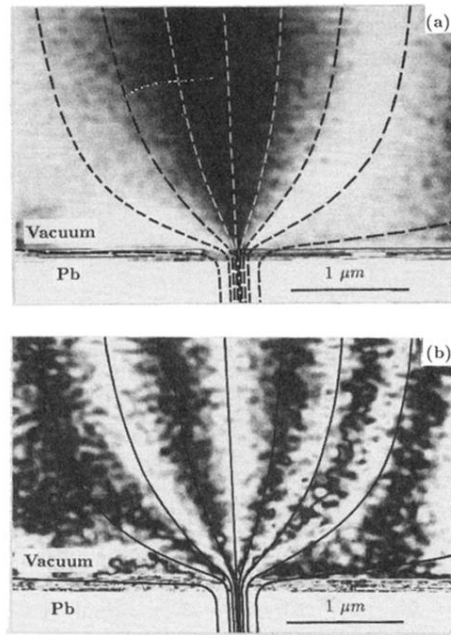


FIG. 14. A singly quantized flux (SQF) line appearing in the 0.2- μm -thick lead film under the 3.7-Oe field. (a) Interference micrograph showing the flux lines in units of $h/2e$, and (b) in units of $h/8e$ (an eight-times phase-difference amplified interference micrograph). The curved dash lines in (a) and the curved solid lines in (b) are the flux distribution calculated from the GL equation Eq. (40) with the Clem model equation (44) using the parameters $\xi = 90 \text{ nm}$, $\lambda = 50 \text{ nm}$.

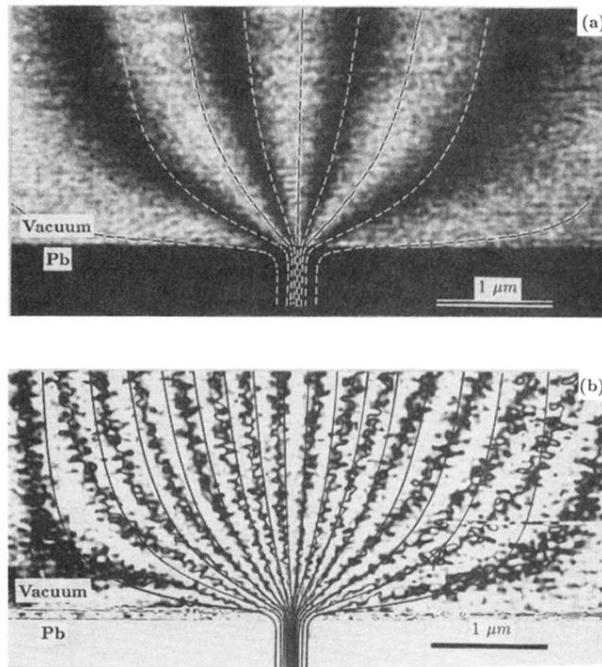


FIG. 15. A multiply quantized flux (MQF- A) line appearing on the $1.0\text{-}\mu\text{m}$ -thick lead film under the 5.0-Oe field. (a) Interference micrograph showing the flux lines in units of $h/2e$ and (b) in units of $h/8e$ (an eight-times phase-difference amplified interference micrograph). The curved dash-lines in (a) and the curved solid lines in (b) are the flux distribution calculated from the GL equation Eq. (40) with the Clem model equation (44) using the parameters $\xi=90\text{ nm}$, $\lambda=50\text{ nm}$.

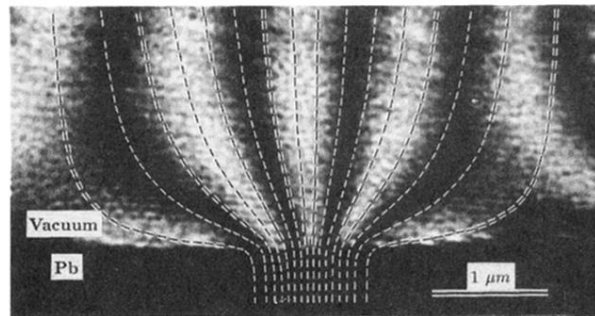


FIG. 16. A multiply quantized flux (MQF- B) line appearing on the $1.7\text{-}\mu\text{m}$ -thick lead film under the 12.2-Oe field. An interference fringe corresponds to the flux quantum $h/2e$. The curved dash lines shows the flux distribution calculated from the GL equation Eq. (40) with a model Eq. (59) with $R=0.4\text{ }\mu\text{m}$, $\xi=90\text{ nm}$, $\lambda=50\text{ nm}$.

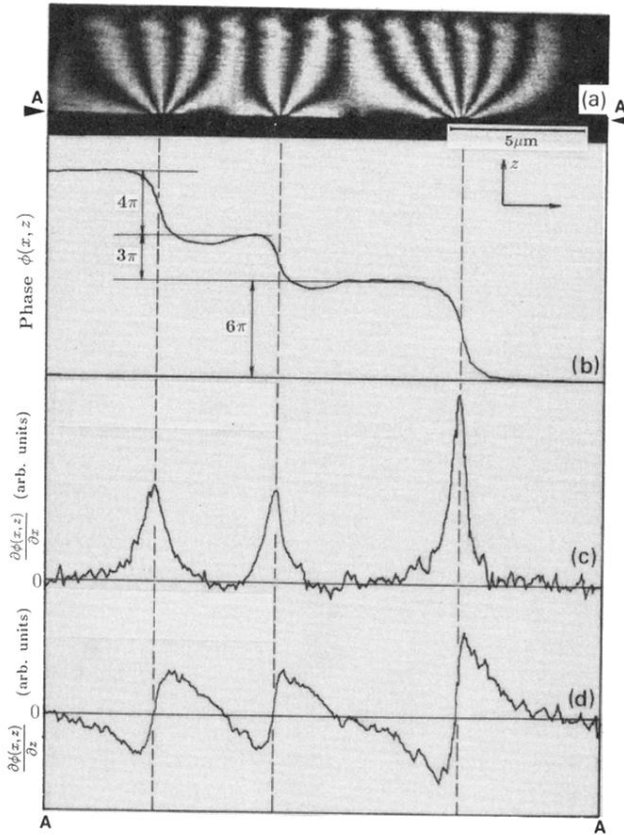


FIG. 17. Digital phase analysis for the fluxes appearing on the $1.0\text{-}\mu\text{m}$ -thick film under the 5.0-Oe field. (a) Interference micrograph showing the MQF- A structure. (b) Line profile of the phase distribution along the line AA just above the superconductor surface in the micrograph (a). (c) Its derivative with x , $\partial\phi(x, z)/\partial x$. (d) Its derivative with z , $\partial\phi(x, z)/\partial z$.

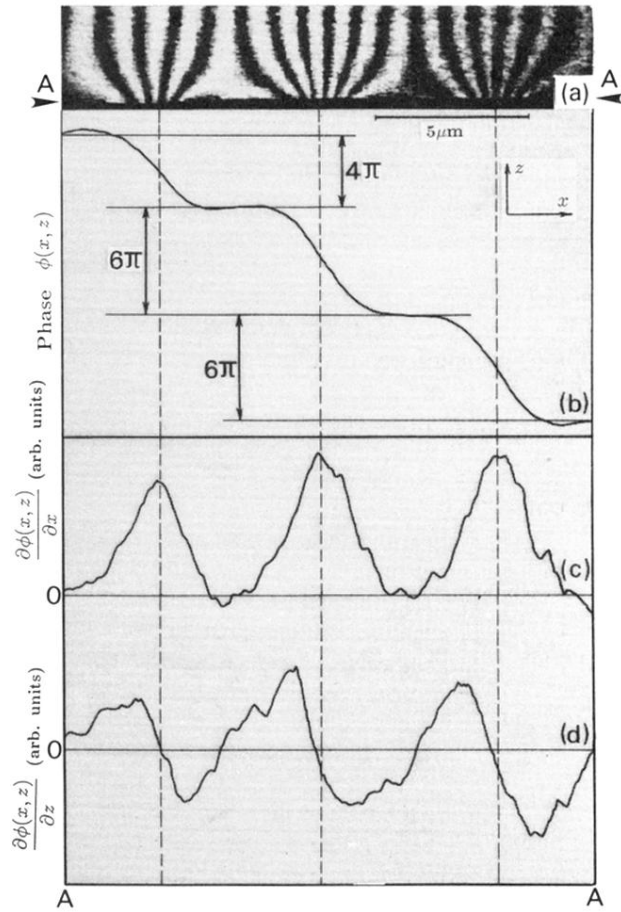


FIG. 20. Digital phase analysis for the fluxes appearing on the 1.7- μm -thick film under the 12.2-Oe field. (a) Interference micrograph showing the MQF-B structure. (b) Line profile of the phase distribution along the line AA just above the superconductor surface in the micrograph (a). (c) Its derivative with x , $\partial\phi(x, z)/\partial x$. (d) Its derivative with z , $\partial\phi(x, z)/\partial z$.

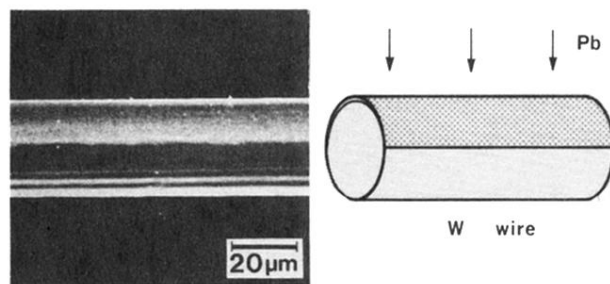


FIG. 3. Scanning electron micrograph of the observation sample. The lead film was deposited on one side of a tungsten wire of $30\ \mu\text{m}$ diameter.